

Heat transfer from wall to dense packing structures of spheres, cylinders and Raschig rings

Moghaddam, E. M.; Foumeny, E.A.; Stankiewicz, A. I.; Padding, J. T.

DOI

[10.1016/j.cej.2020.127994](https://doi.org/10.1016/j.cej.2020.127994)

Publication date

2021

Document Version

Final published version

Published in

Chemical Engineering Journal

Citation (APA)

Moghaddam, E. M., Foumeny, E. A., Stankiewicz, A. I., & Padding, J. T. (2021). Heat transfer from wall to dense packing structures of spheres, cylinders and Raschig rings. *Chemical Engineering Journal*, 407, Article 127994. <https://doi.org/10.1016/j.cej.2020.127994>

Important note

To cite this publication, please use the final published version (if applicable). Please check the document version above.

Copyright

Other than for strictly personal use, it is not permitted to download, forward or distribute the text or part of it, without the consent of the author(s) and/or copyright holder(s), unless the work is under an open content license such as Creative Commons.

Takedown policy

Please contact us and provide details if you believe this document breaches copyrights. We will remove access to the work immediately and investigate your claim.



Heat transfer from wall to dense packing structures of spheres, cylinders and Raschig rings

E.M. Moghaddam, E.A. Foumeny, A.I. Stankiewicz, J.T. Padding*

Process & Energy Department, Delft University of Technology, the Netherlands

ARTICLE INFO

Keywords:

Rigid body dynamics
Particle-resolved CFD simulations
Fixed beds
Raschig rings
Cylinders
Heat transfer
Azimuthal averaging

ABSTRACT

This paper investigates the validity of azimuthal averaging of 3D temperature fields in the analysis of lateral heat transfer in dense particle packings. This is conducted by synthetic generation of 3D packing surrogates of spheres, cylinders and Raschig rings with tube-to-pellet diameter ratio, $3 < N < 6$, using an in-house Rigid Body Dynamics packing algorithm, followed by detailed discrete pellet CFD simulations of heat transfer from wall to bed for laminar, transient and turbulent flow regimes. The CFD results of hydrodynamics and temperature fields are benchmarked against empirical correlations for pressure drop and interphase heat transfer Nusselt number, Nu , offering the best fits with correlations proposed by Einfeld and Schnitzlein (for cylinders and spheres) and Nemeč and Levec (for rings) for pressure drop, and by Gunn and Sun and coworkers for the prediction of Nu . The CFD results demonstrate that fluctuations in local temperature are completely neglected by azimuthal-averaging of 3D temperature fields over the bed volume, leading to more than 150 °C deviations from the local temperature data. Furthermore, it is found that deviations between azimuthally-averaged axial velocity profile and true local velocities are in an analogous fashion transmitted to the temperature field. This is evidenced by the coincidence of the peaks in the deviation profiles of azimuthally-averaged temperature and velocity from the local data over the bed radius. This is due to thermal disequilibrium between fluid and pellet phases which is partially omitted by the azimuthal-averaging of the 3D temperature field and basically neglected in pseudo-homogenous k_{er} - h_w models.

1. Introduction

Tubular fixed bed catalytic reactors with tube-to-pellet diameter ratio, N , in the range of 4 to 10 are extensively employed in process and chemical industries to handle highly exothermic reactions, e.g. oxidation of n-butane to maleic anhydride [1], and endothermic reactions, e.g. methane steam reforming [2], due to enhancing heat transfer from confining wall to the particulate bed. In such narrow-tube reactors, an accurate description of wall-to-bed heat transfer and the positions of hot - or cold - spots inside the tortuous structure is of crucial importance to prevent runaway condition and catalyst deactivation problems during the operation [3]. However, the occurrence of very steep thermal gradients across the tube radius, which is inherent in low- N fixed bed reactors, makes a reliable prediction of transport scalars and reaction rates very problematic at pellet scale [4–9]. Since the 1980s, several research groups have set forth simplistic methodologies founded on 2D quasi-continuum models for *a priori* design of these complicated reactors [10–15]. Such models provide continuous radial and axial profiles of

temperature and concentrations, representing the rates of thermal and material transport across the catalyst bed as being due to an effective single homogenous phase transport rather than distinct solid and gas phase events [16]. As evidenced in literature [5,17–20], the averaged values obtained from pseudo-homogenous models do not suffice to accurately describe the sharp temperature and composition profiles in low- N fixed bed reactor because i) the condition of lateral uniformity of the structures is hardly fulfilled in narrow-tube fixed bed reactors, ii) the plug flow idealization hypothesized in such models obscures the significant roles of flow maldistribution on the local transport processes [19,21–23], iii) these models rely strongly on effective transport parameters which are described in the form of empirical correlations and computed by solving a multi-variable parameter estimation problem to find the best fit with experimental measurements [16]. Nevertheless, these empirical correlations can hardly address the role of pellet's shapes, N and operational conditions and thus are limited in terms of applicability, particularly in low- N fixed bed reactors [5,9]. In addition, several researchers showed the dependency of the effective transport parameters on the bed height, [16,24–26] which can further escalate the

* Corresponding author.

E-mail address: j.t.padding@tudelft.nl (J.T. Padding).

<https://doi.org/10.1016/j.cej.2020.127994>

Received 16 August 2020; Received in revised form 18 November 2020; Accepted 1 December 2020

Available online 8 December 2020

1385-8947/© 2020 The Author(s). Published by Elsevier B.V. This is an open access article under the CC BY license (<http://creativecommons.org/licenses/by/4.0/>).

Nomenclature			
d_o	The outer diameter of rings m	R_t	Bed radius m
d_i	The inner diameter of rings m	Re_p	Reynolds number based on d_{pv} ; $Re_p = \rho v_0 d_{pv} / \mu$ [-]
d_{pv}	Diameter of a sphere of equal volume m	v_o	Inlet velocity $m \cdot s^{-1}$
d_{ps}	Diameter of a sphere of equal specific surface area m	v_z	Azimuthally-averaged axial velocity $m \cdot s^{-1}$
d_t	Tube or bed diameter m	Δp	Pressure drop $kg \cdot m^{-1} s^{-2}$
h	Height of pellet m	r	Radial Coordinate m
I	Turbulence intensity [-]	z	Axial Coordinate m
L	Bed length m	<i>Greek Letters</i>	
N	Tube-to-pellet diameter ratio [-]	ε	Bulk porosity [-]
N_{pv}	Tube-to-pellet diameter ratio based on d_{pv} [-]	$\varepsilon(r)$	Radial porosity profile [-]
N_{ps}	Tube - to - pellet diameter ratio based on d_{ps} [-]	δ	Thickness of Raschig ring mm
Nu	Fluid-to-solid heat transfer Nusselt number; $Nu = h d_{pv} / k_p$ [-]	μ	Fluid dynamic viscosity $kg \cdot m^{-1} s^{-1}$
		ρ	Fluid phase density $kg \cdot m^{-3}$
		Ψ	Dimensionless pressure drop introduced by Eq. (2) [-]

threat of erroneous predictions of temperature and concentrations inside the reactor. With a multiplicity of still outstanding problems associated with the limitations of pseudo-homogenous models as well as discrepancies between predictions and observations [4,9,15], one may presume that applying such models for *a priori* design of low-N fixed bed reactors with strong heat effects are accompanied by some methodical errors that do not stem from faults in the rate equations, but from inherent shortcomings in these models. Thus, even though a rigorous catalyst formulation is devised and approximate operating condition and compositions are identified, such models may offer disappointingly very limited assistance in choosing the optimal pellet size and shape, N and flow rates. To address the local physicochemical phenomena in tubular fixed bed reactors precisely, a spatially resolved 3D simulation is required [17,19–21,27–31]. 3D discrete-pellet Computational Fluid Dynamics (CFD) have been extensively developed during the last two decades [4,29,32]. The merit of this methodology is that it succeeds in capturing many important local flow features and transport properties at pellet-scale in tubular fixed bed reactors [6,18,20,21,28,29,31,33]. Random packing surrogates with different pellet shapes, as a prerequisite for the particle-resolved CFD simulations, have been synthesized using different methodologies such as Discrete Element Methods (DEM) [6,27,29,31,33–37], Monte-Carlo methods [21,22,38], noninvasive image - based method such as MRI [39], and Rigid Body Dynamics (RBD) tools such as the open-source graphical software Blender (which uses the Bullet Physics Library) [40,41] or in-house RBD codes [20]. A detailed review on the prevailing methods for generating particle packing surrogates, including their advantages and disadvantages, has been recently presented by the present authors [23]. Furthermore, alternative strategies have been examined for contact point treatment in such complicated topologies to prevent creation of highly skewed fluid meshes at contact regions, and consequently to enhance convergence in turbulent flow regime simulations. A detailed assessment of the prevailing contact point treatment approaches, viz. global methods including gap and overlap and local methods including bridge and cap, was performed by Dixon et al. [21] and Rebughini et al. [42] in a CFD study of heat transfer in packed columns filled with spheres. The latter authors proposed a meshing protocol to describe the surface reactivity when using bridge method for contact treatment. Up to now, particle-resolved CFD simulations have been extended from detailed flow structure [20,27], mass and heat transfer [9,22,28–30,37,38], to even account for surface-based reactions inside the catalyst bed [43] as well as intra-particle diffusion and reactions [44]. However, the majority of these studies have focused on spheres due to the simplicity of modelling particle packings for such a pellet shape [22,29,37,45,46]. For instance, Guo et al. [29] studied the influence of a free channel, called flow guiding conduit, inside a packed column of spheres on the structural properties, the fluid flow distribution and heat transfer. Kim et al. [46]

compared LES and different RANS models for simulating heat transfer in a fluoride salt-cooled high temperature reactor (FHR) filled with randomly distributed spherical fuel elements. The authors showed that the $k-\omega$ Shear Stress Transport (SST) with low Reynolds number approach gives reasonably good results. Furthermore, they proposed a correlation to predict the Nusselt number for randomly packed heat transferring pebbles in a flowing FLiBe reactor. There are also few publications tackling transport and reactions in fixed beds with non-spherical pellets [19,35,40,47,48]. This scarcity can be attributed to the difficulties with modelling collisions between non-spherical particles [23,49,50] during packing generation. A group of researchers have exercised the glued sphere method to perform DEM-CFD simulations of hydrodynamics, heat and mass transfer and reactions in packed columns of cylinders and Raschig rings [6,35,43]. For example, Wehinger et al. [43] studied the influence of different pellet designs on the conversion of methane dry reforming process. The authors used a glued sphere method in DEM to synthesize random packing of cylinders ($d_p/h = 5/5$ mm) and after further post-treatment in CAD software by making a hole inside the solid cylinders, they constructed a packing surrogate of Raschig rings ($d_o/d_i/h = 6.2/3.5/4.5$ mm) with $N = 3.6$. It is worth noting that this method can only be accurate if the hole diameter is sufficiently small that the (lack of) interpenetration between rings does not affect the bulk porosity of the generated structures [20]. The same approach, i.e. glued sphere in DEM followed by post-treatment in CAD software, was pursued by Dong et al. [6] to generate random packings of steatite rings ($d_o/d_i/h = 6.2/3.5/4.5$ mm with $N = 3.4$). The authors investigated radial heat transfer at moderate flow conditions ($60 < Re_p < 100$). Singhal et al. [35] have investigated the problem of inter-phase heat transfer in fixed beds filled with solid cylinders ($d_p = 1$ mm with aspect ratio from 2 to 6) using particle resolved direct numerical simulation (PR - DNS). The authors used Star CCM⁺ 11.02, a commercial DEM package, to synthesize a packing surrogate of cylinders using the glued-sphere method. Based on the simulation results, they proposed a correlation for fluid-to-particle heat transfer Nusselt number. There are a few studies that use a hard body approach based on Rigid Body Dynamics (RBD) to synthesize random packings of non-spherical particles followed by a supplementary CFD study to analyze local behavior of flow structure and heat and mass transfer in fixed bed reactors [20,40,48,51]. The pioneering works are the contributions of Boccardo et al. [40] who used the open-source code Blender (a graphical software which uses the Bullet Physics Library) to generate packed columns of different pellet shapes such as spheres, cylinders, and trilobes for the study of hydrodynamics, and Moghaddam and Farbod [52], who developed an in-house RBD code to synthesize random packings of cylinders for the study of hydrodynamics and heat transfer. Following these research efforts, Partopour and Dixon [48] have presented a tailor-made integrated workflow using the Bullet Physics Library for computational generation of randomly packed

particulate structures of arbitrary-shaped pellets. The authors examined their automated package for the analysis of flow and pressure drop in random packings of spheres, cylinders, Raschig rings, and quadrilobes with five holes. In our previous contribution [20] we used our sequential RBD - CFD method to investigate the local flow structure, the inadequacy of azimuthal averaging of velocity field and the role of wall-effects on flow maldistribution and pressure drop in tubular fixed beds of equilateral cylinders. In this work, we report on the results of detailed 3D discrete-pellet CFD simulations of the heat transfer from wall to dense particulate beds. Simulations are conducted for dense packing structures of spheres, equilateral solid cylinders and Raschig rings with N ranging from 3 to 6 for a wide range of Re_p values. We will show the importance of structural heterogeneity, the validity of azimuthal averaging of the temperature field, the correlation between the in-situ behavior of velocity and temperature distributions in 3D and 2D schemes, and the roles of wall-effect and pellet design on the lateral heat transfer rate in a wall-heated narrow-tube fixed bed heat transfer problem. An effort will be made to cast some light on the reasons behind the methodically-driven deviations of radial temperature profile, obtained from k_{er-h_w} pseudo-homogenous heat transfer model, from the pellet-scale temperature field.

2. Discrete – Pellet RBD-CFD modelling

2.1. RBD modeling of packing structures

The synthetic generation of random packing surrogates of spheres, equilateral cylinders and Raschig rings is conducted using our recently published RBD-based packing algorithm [23]. The RBD-algorithm is implemented as an in-house C++ code, in which i) the surface of non-spherical pellets is modeled by very fine triangular face meshes based on the robust and fast subdivision-based polygonal approach by Loop [53], ii) a hard body approach is exerted to handle collision phenomena, i.e. colliding contacts and resting contacts, iii) the transition between moving and resting pellets is controlled by a cutoff on the relative contact velocities to stabilize the convergence in packing simulations. Details of the methodology, together with verification and validation studies, are presented in the original paper [23]. In this work, a reactor tube is represented by a simple open-top empty cylinder (with a height of 150 mm and different diameters, see Table 1) which is modeled by triangular face meshes. A preset number of pellets, i.e. spheres, cylinders

Table 1
Pellet properties and settings used in RBD simulations for packing generation.

Case studies and parameters	Preset value	
Case study 1: Spheres	Pellet size [mm]	$d_p: 10$
	Tube diameter, d_t , [mm]	31, 41, 61
	Number of face mesh per pellet [#]	3120
Case study 2: Cylinders	Pellet size [mm]	$d_p/h_p: 10, d_{pv}: 11.45$
	Tube diameter, d_t , [mm]	22.9, 35.5, 45.8
	Number of face mesh per pellet [#]	4400
Case study 3: Raschig rings	Pellet size [mm]	$d_{po}/d_{pi}/h_p: 10/6/10, d_{pv}: 9.87$
	Tube diameter, d_t , [mm]	30.6, 40.5, 60.2
	Number of face mesh per pellet [#]	8008
Pellet density [$kg \cdot m^{-3}$]	8030	
Surface friction coefficient of pellets (dynamic)	0.1	
Surface bounciness of pellets (COR*)	0.9	
Surface friction coefficient of tube walls (dynamic)	0.6	
Surface bounciness of tube wall (COR*)	0.6	
Gravity acceleration [$m \cdot s^{-2}$]	9.81	
Integration time step [s]	0.0025 and 0.025	

Note: * COR: Coefficient of Restitution

and Raschig rings, are then placed at the top of the tube and in a column in line with the tube axis, viz. cylinders and rings are placed obliquely with an angle of 45° with respect to the gravity direction, and fall freely under the gravitational field to the bottom of the tube (see [23] for more details). A force-torque balance, together with other auxiliary models accounting for pellet-pellet and wall-pellet interactions, i.e. collisional contacts and resting contacts, is solved for each pellet over a preset time to simulate the particle loading process. The particle packing simulation stops when a dynamic equilibrium based on the work-energy theory is reached. Since the resulting mean and local porosities of the RBD-simulated structures are strongly influenced by the physio-mechanical properties of pellets and container, tube-to-pellet diameter ratio and the loading method, we pursued the setup procedure presented in our previous work [23] to synthesize the densest possible random packings of spheres, cylinders and Raschig rings. Details of the pellet properties and settings used in the RBD simulations are given in Table 1. Typical computer-generated random packings of spheres, cylinders and Raschig rings with N_{pv} (tube-to-pellet diameter ratio based on the sphere diameter of equivalent pellet volume) around 4 are illustrated in Fig. 1.

2.2. Computational domain and meshing procedure

The geometrical details of the RBD-generated structures, including the positions of the barycenters together with the surface face vertices of each pellet are imported to ANSYS Workbench 16.2 to produce a CAD model of the packing structure. The pellets are then shrunk by 0.5% around their center of mass. This results in very small interstices at the contact points, edges and faces, and thereby prevents highly skewed cells in such regions. The size of the created gap is sufficiently small to have a negligible impact on the bulk and local porosities of the generated packings, and to prevent jet formation within the gaps even at high Re_p flow conditions according to Dixon et al. [54] and Bai et al. [34]. The minor effect of this post-treatment on the bulk porosity of the generated structures is investigated quantitatively in section 3.1. The described contact point treatment method allows for an advanced meshing approach based on a combination of patch-independent and patch-conforming meshing methods to generate a high quality



Fig. 1. RBD-generated structures for spheres, cylinders and Raschig rings with $N = 4.1, 4.58$ and 4.05 , respectively.

inflationary mesh topology in the dense packing structures. This is performed by an ad-hoc Python script in ANSYS Workbench 16.2, which creates very fine meshes at the contact regions evolving into coarser tetrahedral grids in the bulk of voids and pellets through a graded meshing scheme. Further details can be found in Moghaddam et al. [20]. A precise prediction of the local velocity and temperature surface boundary layers occurring in turbulent flow simulations requires devising a number of prismatic layers on the surface of pellets and tube walls [18,21,55]. Our boundary layer treatment for the turbulent flow regime simulations comprises of six layers of prisms with an initial height of 2.5×10^{-6} m and a growth factor of 1.2 of thickness per layer along the surface normal direction. This allows the laminar sub-layer to be accurately resolved even for the cases with the sharpest velocity and temperature gradients at highest inlet Re_p by obtaining the recommended dimensionless distance parameter, i.e. $y^+ \approx 1$, according to the Enhanced Wall Treatment (EWT) method. Furthermore, considering a very fine mesh in the contact areas leads to a very smooth growth in the mesh topology from the boundary layer regions to the void and solid bulk zones inside the packing structures, thereby facilitating the convergence in turbulent flow simulations without any need for manipulating the under-relaxation factors. Figs. 2 and 3 illustrate typical results of face mesh quality (aspect ratio) for packings of spheres and cylinders and typical results of inflationary mesh scheme at different cut plains in packing structures of spheres, cylinders and rings, respectively, with $N_{pv} = 3.1$.

2.3. CFD model description and implementation

Discrete-pellet CFD simulations of hydrodynamics and heat transfer are conducted. Packing models with different pellet shapes and tube-to-pellet diameter ratios (see Table 1) are scrutinized, in the laminar, transitional and turbulent flow regimes, using the finite volume code ANSYS Fluent 18.2. The simulations are in steady-state mode and the fluid phase is assumed to be Newtonian, incompressible and non-isothermal with the physical properties of air. Furthermore, the ideal gas law and Sutherland's law are employed to account for density- and viscosity-temperature dependencies, respectively. To investigate the influence of catalyst pellets of different thermal conductivities on the wall-to-bed heat transfer, the thermal conductivity of the pellets is set as 1.01, 16.27 and 40 W/m.K, corresponding to glass, steel and alumina catalyst material, respectively.

The air at the inlet has a total pressure of 1.01325 bar and temperature of 298 K, which gives the physical properties of $\rho = 1.225 \text{ kg/m}^3$, $c_p = 1006.43 \text{ J/kg.K}$, $k_f = 0.0242 \text{ W/m.K}$, $\mu = 1.7894 \times 10^{-5} \text{ Pa.s}$ (yielding a molecular Prandtl number of 0.74). The air enters from the

bottom of the packed tube with uniform axial velocity and temperature to provide a constant basis for further comparisons and analyses. A velocity-inlet boundary condition is chosen, with axial velocity consistent with the desired Re_p (based on the volume-equivalent pellet diameter) ranging from 5 to 3000. For transient and turbulent flow simulations (for $Re_p \geq 600$), the initial inlet turbulence intensity is estimated based on the formula $I = 0.1Re_p^{-1/8}$ to provide a similar basis for CFD simulations. The thermal boundary condition at the tube wall is considered as constant temperature ($T_w = 700 \text{ K}$ for $Re_p \leq 200$ and $T_w = 1500 \text{ K}$ for $Re_p \geq 400$). No-slip boundary conditions are applied to the tube wall and pellet surfaces, i.e. at fluid/solid interfaces. Furthermore, a coupled heat transfer boundary condition is applied to the fluid/pellets interfaces to account for conjugate heat transfer. ANSYS Fluent uses a discrete form of Fourier's law to compute the fluid/solid film heat transfer at a pellet surface in the laminar flow regime. However, for turbulent flow, the law-of-the-wall (defined by a wall function, which here is Enhanced Wall Treatment) together with the analogy between heat and momentum transfer is applied. Furthermore, the reactor tube is extended by 1 and 6 particle diameters at the bed inlet and outlet, respectively, to minimize the tube ends boundary effects on tortuous flow structures. Fig. 4 shows a schematic overview of the flow model and boundary conditions.

The governing equations for CFD simulations of wall-to-particulate bed heat transfer include the three-dimensional compressible Navier-Stokes and energy equations for the laminar flow regime ($Re_p \leq 100$). For the fully-turbulent flow regime, i.e. for $Re_p \geq 600$, the realizable k- ϵ model combined with the Enhanced-Wall-Treatment (EWT) is applied, which basically is a tried-and-tested RANS model for simulating velocity and temperature fields with strong streamline curvature, see e.g. [6,20,21,27,29]. It is worth mentioning that for the inlet Re_p ranging from 100 to 600, where the transition from laminar to turbulent flow occurs, both the (laminar) Navier-Stokes equations and the realizable k- ϵ model are examined.

The governing equations are solved using pressure-based segregated solver in ANSYS Fluent 18.2, with the SIMPLE scheme for pressure-velocity coupling. The interpolation scheme used for computing the cell-face pressures is the PRESTO! (PREssure STaggering Option) method, which is a recommended method for problems with strong body forces (swirl) and high Rayleigh number flows. A second-order upwind interpolation scheme is applied for both the convection and diffusion terms to interpolate the field variables (stored at cell centers) to the faces of a control volume. Furthermore, the gradients of solution variables at cell centers are determined using a Green-Gauss node-based method to minimize false diffusion. The CFD runs are initially set under isothermal conditions with only momentum and turbulence activated. Having

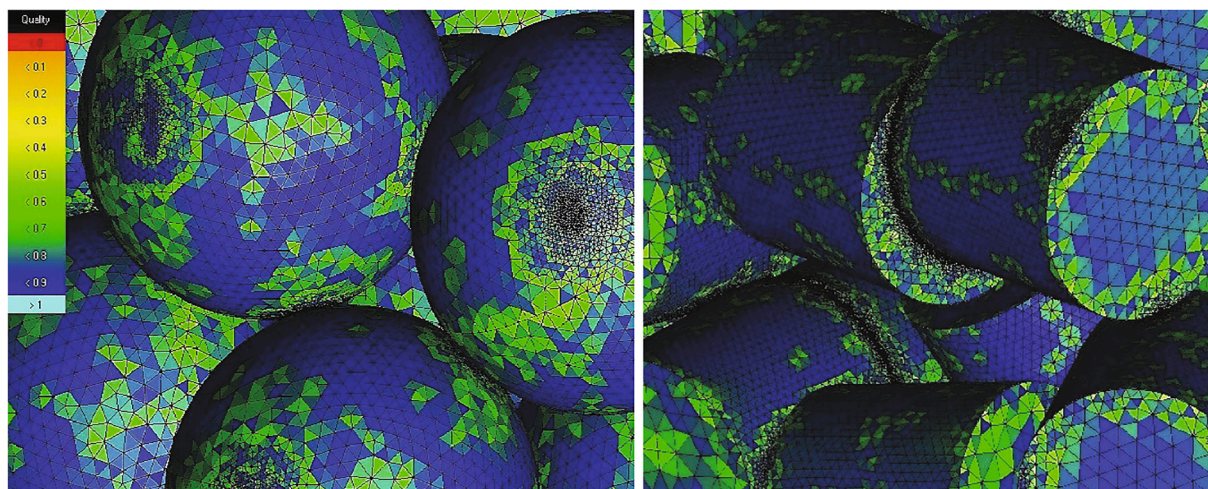


Fig. 2. The face mesh quality (aspect ratio) of pellet surfaces based on a medium mesh size (see Table 2) for packings of spheres and cylinders.

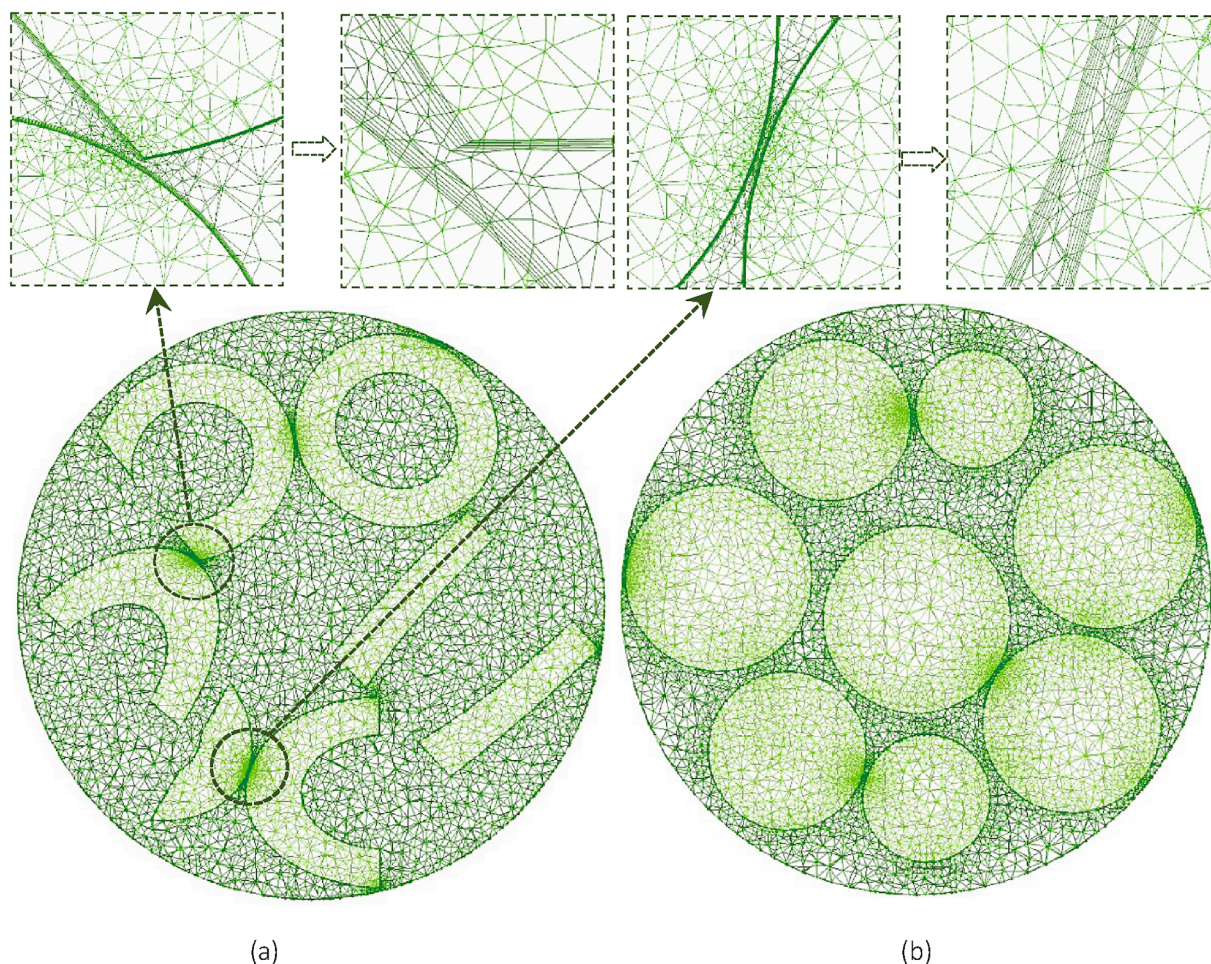


Fig. 3. Typical results of graded mesh topology generated based on the medium mesh size (see Table 2) in different packings with $N_{pv} = 3.1$. (a) a cut plane of the volume mesh at height $z = 7d_p$ together with a zoom-in at typical proximity zones; (b) a cut plane of the volume mesh at height $z = 5d_p$.

established a converged flow field throughout the computational domain, the heat transfer simulations are run by setting the thermal boundary conditions and the temperature-dependent properties of the flowing fluid. Contrary to previous works e.g. [21,48,54,56], convergence can be properly achieved without a need for manipulating the under-relaxation factors which can be ascribed to the very high-quality mesh topology created using the advanced method outlined earlier in section 2.2.

3. Verification and validation study

3.1. Bulk and local bed porosities

The first important step of the post-processing analysis is to characterize and inspect the validity of the RBD-generated packing structures. To validate the RBD simulation results, the bulk porosity and radial void fraction distribution obtained from the models are benchmarked against literature data. The bulk voidage of all simulated structures before and after contact point treatment is compared with literature data in Table 2.

The resulting bulk voidages demonstrate a reasonable agreement with the empirical correlation by Dixon [57] for all packing models. The contact point treatment, i.e. local shrinking of pellets by 0.5%, leads to some minor changes in the bulk voidage of the RBD-generated structures within the ranges of 1.7% to 2.2% for sphere packings, 0.5% to 2.3% for cylinder packings, and 0.6% to 1% for Raschig ring packings (see Table 2). These alterations are sufficiently minor to not affect the local

flow structure and the bed hydrodynamics according to Bai et al. [34].

In our previous study on the hydrodynamics of low- N fixed beds of spheres and cylinders [20], the radial void fraction profiles, $\varepsilon(r)$, obtained from the conceptual models were investigated and validated against literature data and correlations. Therefore, here only the axially-averaged radial porosity distributions for packings of Raschig rings are presented, see Fig. 5, wherein $\varepsilon(r)$ is depicted versus the dimensionless wall distance. It is worth mentioning that the number of concentric tubes used for sampling the radial void fraction varies in respect to N , resulting a sampling intervals within the range of $0.09d_{pv}$ to $0.135d_{pv}$ for all cases.

As shown in Fig. 5, the radial porosity profiles in random packings of Raschig rings demonstrate a quite distinct pattern, which is different from that of packings of spheres and cylinders. The observed pattern can be characterized by a series of humps, which stem from the presence of a hole inside the Raschig ring pellets, repeating in a damped-oscillatory fashion towards the center of the bed. The first peak occurs at a distance of $0.5d_{pv}$ from the tube wall, which is a little shifted towards the container wall compared to the position of the first minimum in the radial void fraction profiles in random packings of full (solid) cylinders, i.e. $0.65d_{pv}$, reported in our previous study [20]. This observation can be explained by the interpenetration of Raschig ring pellets due to the presence of a hole inside such pellets, affecting the ordering of the positions of pellets along the tube radius. It is worth noting that the results show the presence of a channel along the bed axis for a Raschig ring packing with $N = 3.1$. Such topological behavior, which is a consequence of restrictive structuring effects by the tube wall for specific values of N , has been previously observed for random packings of

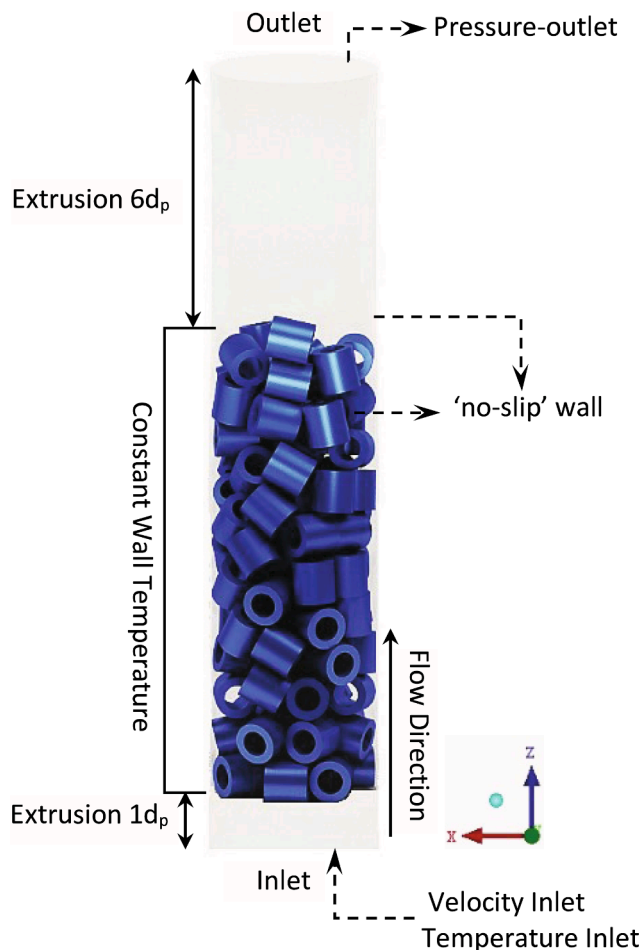


Fig. 4. Schematic overview of the CFD flow model and boundary conditions used in the discrete-pellet CFD simulations represented by a tube stacked with Raschig rings pellets with $N_{pv} = 3.1$.

Table 2

Bulk voidage of RBD-generated packings.

Pellet shape	N(d_p / d_p)	Bulk porosity analysis (based on packing height of H = 120 mm)			Bulk porosity (after shrinkage)
		RBD-gen. packings	Dixon [57]	MRE (%)	
Sphere	3.1	0.462	0.459	-0.65	0.470
	4.1	0.435	0.437	0.46	0.443
	6.1	0.409	0.419	2.38	0.418
Cylinder	2.29	0.580	0.585	0.85	0.583
	3.55	0.477	0.465	-2.60	0.485
	4.58	0.386	0.429	9.97	0.395
Raschig rings	3.06	0.695	0.652	6.59	0.699
	4.05	0.641	0.626	2.43	0.647
	6.02	0.601	0.605	-0.77	0.607

spheres with $N = 4$, see [20,22,27,58], and cylinders with $N = 4.58$, i.e. $N_{pv} \approx 4$ [20].

3.2. Mesh verification study

A mesh independency study was conducted based on three different levels of mesh size implemented in the narrowest packing model of cylinders with $N = 2.29$, in which the sharpest gradients are anticipated. The mesh size range together with the cell counts are given in Table 3.

The CFD results of the velocity and temperature distributions are

compared in Fig. 6 for the three mesh levels along the tube diameter on x-axis at bed height $z = 100$ mm and $Re_p = 10000$. Furthermore, Fig. 7 shows the azimuthally-averaged temperature profile at different bed cross sections, together with the local temperature data along the bed axis for the same Re_p , where the sharpest temperature gradients are expected. Overall, the obtained results demonstrate reasonable agreement between medium and fine mesh sizes for the computed axial velocity and temperature profiles. The inadequacy of the coarse mesh can be evidently discerned, predominantly at the wall regions, where the gradients are essentially steeper, leading to underestimation of the velocity and temperature profile at the bed center zone.

The Richardson extrapolation (RE) method (Roache [59]) was used to quantitatively evaluate the discretization error of the medium mesh level for the computed velocity and temperature fields. The RE approach uses the field variables computed based on the medium mesh, δ_m , and the fine mesh, δ_f , sizes to extrapolate the values that would theoretically be obtained at zero mesh size, δ_∞ , (see eqs. (1), (2)).

$$\delta_\infty = \delta_f + \frac{\delta_f - \delta_m}{r_g^2 - 1} \quad (1)$$

$$r_g = \sqrt{\frac{N_f}{N_m}} \quad (2)$$

where N_f and N_m are mesh sizes of the fine and medium meshes, respectively. This formula assumes a second order discretization error. The extrapolated relative error (ERE) for the medium mesh can then be expressed by:

$$ERE = \left| \frac{\delta_\infty - \delta_m}{\delta_\infty} \right| \quad (3)$$

This approach was applied to the CFD results of pressure at $Re_p = 10,000$ and azimuthally-averaged temperature profile (Fig. 7a) for fine and medium mesh levels to predict the value of bed pressure drop and temperature profile at zero grid size, i.e. Δp_∞ , $T(r)_\infty$. Using this method, the numerical error was computed as 1.77% for pressure drop and the average errors for the radial temperature profiles at $z = 100$ and 180 mm were estimated as 1.74% and 1.03%, respectively. With this, we deem the medium mesh size to be sufficiently accurate for all remaining CFD simulations.

3.3. Pressure drop

The validity of the hydrodynamics predicted by the CFD simulations was assessed by comparing the predicted pressure drop along the particulate beds to literature correlations. Different modifications of the constants of the Ergun equation to account for wall-effects and pellet shape were examined in this comparison study (see Table 4 for references). Here, the pressure drop is represented in dimensionless form, the so-called pore-based friction factor, which is expressed as:

$$\Psi_w = \frac{\varepsilon^3}{1 - \varepsilon} \frac{\Delta P}{\rho u_s^2} \frac{d_{ps}}{L} \frac{1}{M} = \frac{A_w}{Re_w} + B_w \quad (4)$$

$$M = 1 + \frac{2}{3N(1 - \varepsilon)} \quad \text{and} \quad Re_w = \frac{\rho_f u_s d_{ps}}{\mu(1 - \varepsilon)M} \quad (5)$$

Table 4 summarizes the noted constants A_w and B_w for some of the mostly-used correlations for predicting pressure drop in tubular fixed bed systems.

Fig. 8 shows the computed dimensionless pressure drop, Ψ_w , expressed by eqs. (4), (5), obtained from numerical simulations of different packing structures for a bed height of 100 mm, compared with predictions by several correlations.

Overall, as illustrated in Fig. 8, the numerical results show good agreement with the empirical correlations in all flow regimes for packings of spheres with $N = 6.1$, cylinders with $N = 4.58$ and Raschig rings

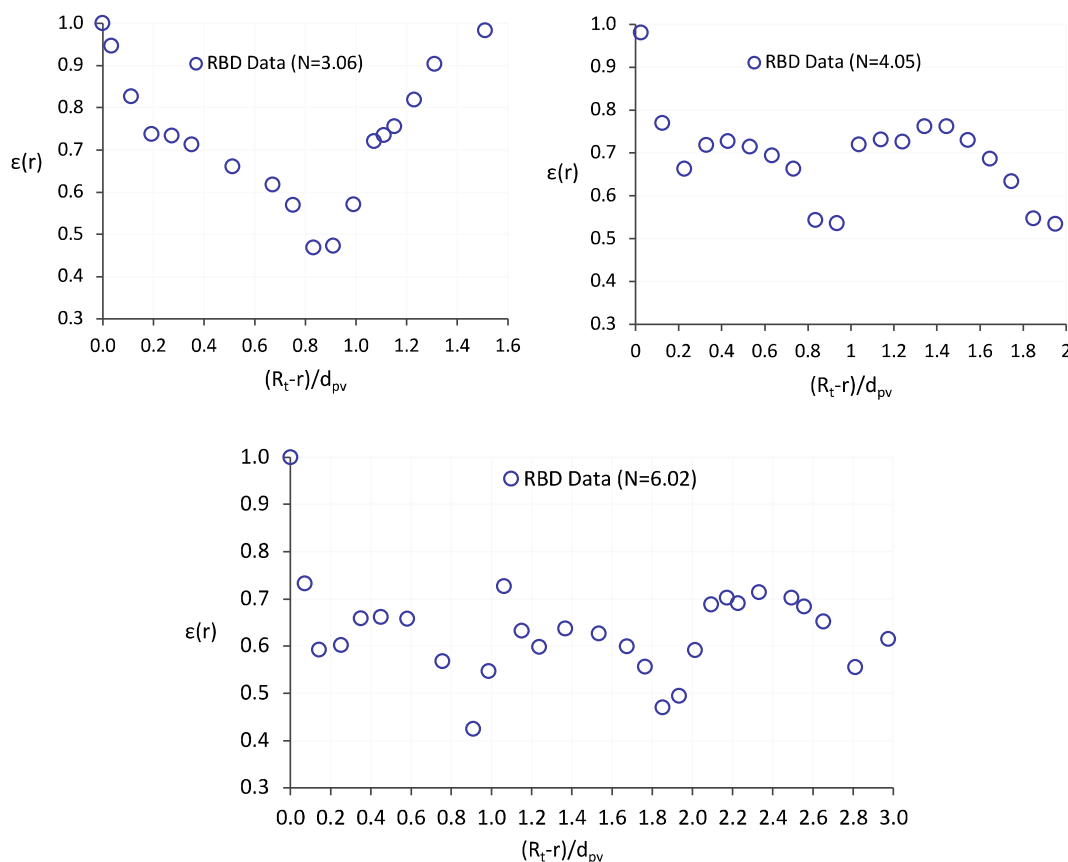


Fig. 5. Radial porosity distribution obtained from RBD - generated packing models of Raschig rings for different tube-to-pellet size ratios N . Note that the horizontal axis shows the dimensionless distance to the wall.

Table 3

Mesh verification study settings, the cylindrical packing with $N = 2.29$.

Description	Fine	Medium	Coarse
Mesh size range (mm)	0.05–0.4 (d_p /25)	0.05–0.55 (d_p /18.2)	0.05–0.8 (d_p /12.5)
Fluid Cells ($\times 10^6$)	15.29	10.87	6.80
Total cells ($\times 10^6$)	23.27	17.70	10.04

with $N = 6.02$. Similar results were obtained for packing models with other N values, but not shown here for sake of brevity. Furthermore, very good agreement was found with the modifications proposed by Einfeld and Schnitzlein [63] for packing models of spheres and cylinders and by Nemeč and Levec [66] for packings of Raschig rings (see Table 5). The deviations from the correlations reported in Table 4 are evaluated based on mean relative errors, MRE, and reported in Table 5 for all packing models.

The largest deviations from the modified Ergun equation can be found in packings of Raschig rings, implying that even with the use of the equivalent particle diameter, i.e. d_{ps} , to account for the effect of the pellet's shape, the Ergun model underestimates the pressure drop. This can be attributed to the role of the hole inside such pellets, providing additional dead zones and source for eddy formation inside the particulate bed compared to spheres, which cannot be compensated with a larger specific surface area of the rings. This, therefore, results in a higher pressure drop in Raschig ring packings than those predicted by the modified Ergun equation (see Fig. 8c).

It is worth mentioning that for $Re_p > 600$, which is the typical flow condition of heterogeneous catalytic flow reactors in process industries, the MRE% computed based on Einfeld and Schnitzlein [63] for the packing models of spheres and cylinders and from Nemeč and Levec

[65] for the packings of Raschig rings becomes lower than 10.6%, evidencing the reliability of these correlations for the use in engineering design calculations.

3.4. Fluid-to-pellet heat transfer coefficient

The results of heat transfer simulations were validated by comparing the computed fluid-to-solid heat transfer coefficient represented by the Nusselt number, $Nu = hd_p/k_p$, to values extracted from the often-cited literature correlations. Some of such typical correlations used in the analysis are given in Table 6.

The fluid-to-solid heat transfer coefficient h plays an important role in heterogeneous heat transfer models, wherein interphase thermal resistances are so significant that the particulate bed system can no longer be treated as a quasi-continuum system, and consequently cannot be modeled using pseudo-homogenous models with effective parameters. The interphase heat transfer coefficient can be obtained from our numerical experiments by an appropriate lumping proposed by Stuke [73]. The author demonstrated that h should be treated as a lumped parameter comprising of fluid/solid film heat transfer coefficient, h_{fs} , and the solid (catalyst) phase thermal conductivity, and hence proposed the following formula:

$$\frac{1}{h} = \frac{1}{h_{fs}} + \frac{d_p/\beta}{k_p} \quad (6)$$

where $\beta = 10, 8$ and 6 for spheres, cylinders, and slabs, respectively. To obtain the fluid/solid film heat transfer coefficient, h_{fs} , from the CFD results, the facet-averaged value of total heat flux for the solid phase, q'_{fs} , is computed and then divided by the difference between the mass-weighted average fluid phase temperature, $T_{f,b}$, and the face-averaged temperature at the pellets' surface, $T_{p,s}$.

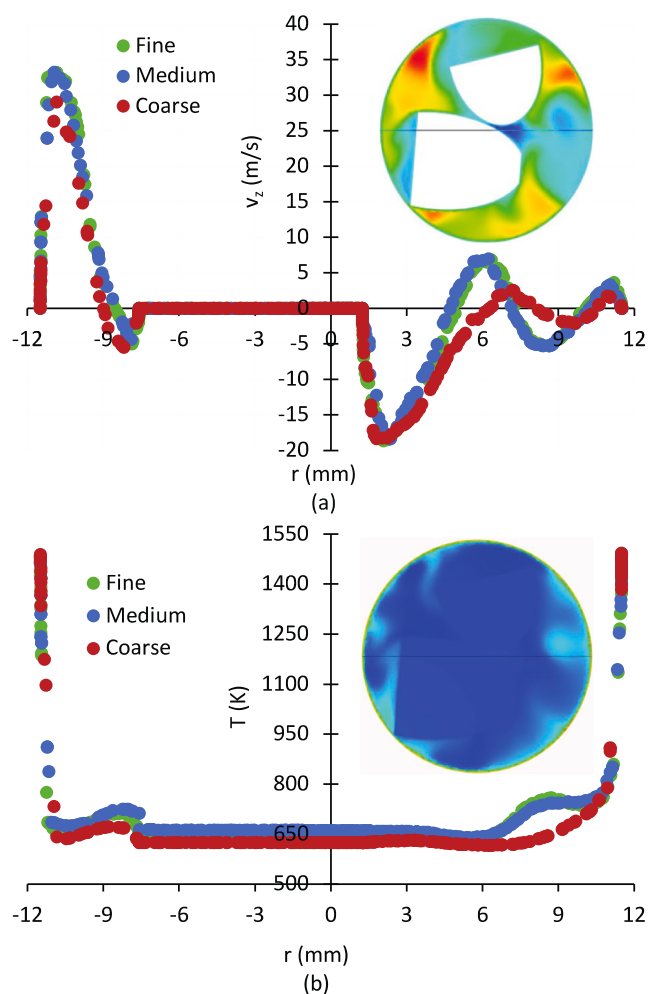


Fig. 6. Comparison between computed (a) axial velocity profiles, and (b) temperature profiles, based on three mesh levels at a typical line passing through the points $(-0.0115, 0.11 \text{ m})$ and $(0.0115, 0.11 \text{ m})$ in a cylindrical packing with $N = 2.29$ and $Re_p = 10000$.

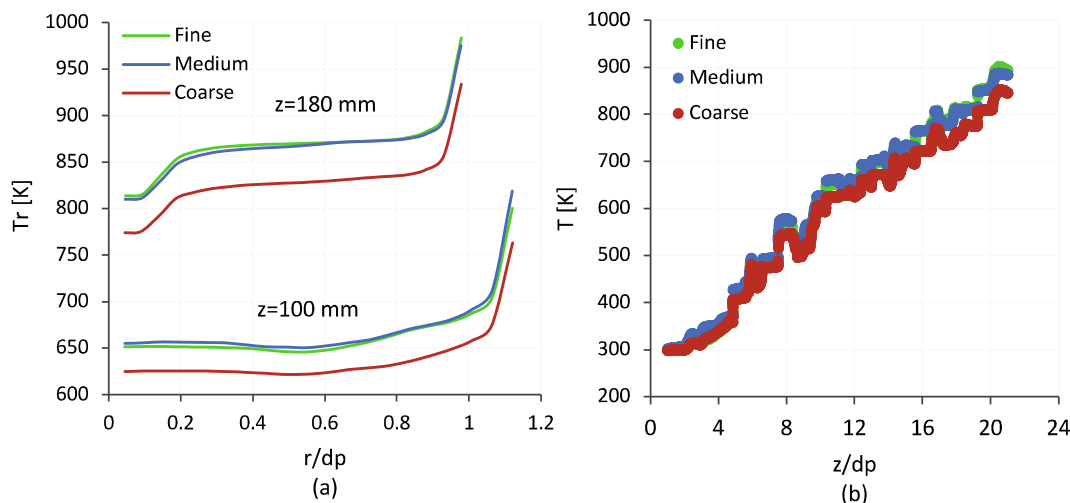


Fig. 7. Comparison between computed temperature profile obtained from three mesh levels in a cylindrical packing with $N = 2.29$ and $Re_p = 10000$; (a) azimuthally-averaged temperature profile at $z = 100$ and 180 mm , (b) local temperature data along the bed axis.

$$h_{fs} = \frac{q'_{fs}}{T_{f,b} - T_{p,s}} \quad \text{and} \quad Nu_{fs} = \frac{h_{fs} d_{pv}}{k_f} \quad (7)$$

$$T_{f,b} = \frac{\sum_{i=1}^n T_{f,i} \rho_i |V_i|}{\sum_{i=1}^n \rho_i |V_i|} \quad (8)$$

$$\varphi = \frac{\sum_{i=1}^n \rho_i \varphi_i}{n} \quad \text{where } \varphi : q'_{fs} \text{ and } T_{p,s} \quad (9)$$

where V_i and ρ_i are the volume and fluid density in cell i located in the fluid domain.

Furthermore, correlations were also defined as custom field functions in ANSYS Fluent, thereby accounting for the mass-weighted average of Re_p and Pr from the fluid phase.

As shown in Fig. 9, the computed Nusselt number and the correlation results are in satisfactory agreement in all flow regimes for packings of spheres with $N = 3.1, 6.1$. Similar results were obtained for packing models with other N values, not shown here for the sake of brevity. Furthermore, results demonstrate very good agreement with correlations proposed by Gunn [70] and Sun et al. [72], resulting in mean relative errors lower than 13%.

4. Results and discussion

4.1. Contour maps of velocity and temperature fields

The analysis of heat transfer in tubular fixed beds is essential, as it can strongly influence the reactor performance in terms of product yield and selectivity. In lower N -beds, say $N < 10$, confinement by the reactor wall induces a radial heterogeneity in the local packing structure. The consequence of such a topological feature can strongly impact the local flow structure and accordingly the lateral temperature distribution. Fig. 10 illustrates three examples of velocity and temperature fields in both fluid and catalyst phases, in the form of contour maps of axial velocity normalized by the inlet velocity and temperature for several cross sections for packings of spheres, cylinders and Raschig rings with $N_{pv} = 3.1$ and $Re_p = 100$.

The contour maps of normalized axial velocities and temperature fields at three different bed cross sections show significant inhomogeneity in the local velocity and temperature distributions along packing depth, which stems chiefly from the substantial spatial heterogeneity inherent in such low- N packing structures. The observed local inhomogeneity in temperature field is much more discernable in packings of cylinders and Raschig rings, closely connected to the sharp edges

Table 4
Empirical correlations proposed for evaluating A_w and B_w used in eq. (4).

Authors	A_w	B_w	N	Re_p
Mehta & Hawley [60]	150	1.75	7.7 ~ 91	0.18 ~ 9.55 ^a
Reichelt [61]	150 for sphere 200 for cylinder	$[1.5N^{-2} + 0.88]^2$ for sphere $[2N^{-2} + 0.80]^2$ for cylinder	1.7 ~ 91	74 ~ 5463
Foumeny et al. [62]	$\frac{130}{M^2}$ for sphere	$\frac{N}{M(2.28 + 0.335N)}$	3.23 ~ 23.8	28 ~ 4569
Eisfeld & Schnitzlein [63]	154 for sphere 190 for cylinder 150 for all particles	$[1.15N^{-2} + 0.87]^2$ for sphere $[2N_{ps}^{-2} + 0.77]^2$ for cylinder $[1.42N_{ps}^{-2} + 0.83]^2$ for all particles	1.62 ~ 250	0.07 ~ 17,625
Montillet et al. [64]	$\frac{1000\alpha}{M^2(1-\epsilon)} N^{0.2}$ for sphere where $\alpha = 0.061$ & 0.05 for dense and loose packings, respectively	$\frac{12\alpha}{M} N^{0.2}$ for sphere	3.8 ~ 14.5	11 ~ 2557
Nemec and Levec [65]	$\frac{150}{\phi_s^{1.5} M^2}$ for cylinder $\frac{150 \times \mathfrak{N}}{M^2}$ for Raschig rings where $\mathfrak{N} = \left[\frac{\epsilon^3}{(1-(1-\epsilon)(V_s - mV_i)/V_p)^3} \right] \times \left[\frac{(S_f + mS_i)}{V_p} \frac{d_{ps}}{6} \right]_b$	$\frac{1.75}{\phi_s^{1.33} M}$ for cylinder $\frac{1.75 \times \mathfrak{N}}{M}$ for Raschig rings	2.15 ~ 7.89	1 ~ 1000 ^a
Cheng [66]	for spheres $\left[185 + 17 \frac{\epsilon}{(1-\epsilon)} \left(\frac{N}{N-1} \right)^2 \right] \frac{1}{M^2}$	for spheres $\left[1.3 \left(\frac{\epsilon}{1-\epsilon} \right)^{1/3} + 0.03 \left(\frac{N}{N-1} \right)^2 \right] \frac{1}{M}$	1.1 ~ 50.5	2 ~ 5550

^a The range of $Re/(1-\epsilon)$ was reported in the original papers.

^b According to the corrections proposed by Sonntag [67] for Raschig rings pellets, reformulated in the form of Ergun constants.

of the cylinders and rings which impose stronger curvatures of the streamlines along the packing. Similar observations and deductions can be attained from other studies [6,20,74,75]. Furthermore, the temperature contour maps at each cross section show that there is no azimuthal symmetry in temperature distribution, which is due to the extreme radial and angular heterogeneity inherent in the structures of low-N beds. These results can also explain why the use of a 120° wall-segment packing model is not adequate for CFD analysis of flow and heat transfer in a full narrow-tube fixed bed, because the role of angular heterogeneity of bed structure is completely omitted in two-thirds of the bed cross section.

The contour plots of the flow field in Raschig ring packings demonstrate a totally different flow structure than in the other two types of packing. Raschig rings oriented parallel to the flow allow for acceleration of the local velocity through their axial holes, while rings oriented perpendicular to the flow provide additional space for vortex formation. This behavior can cause a higher level of inhomogeneity in the temperature field compared to those found in packings of cylinders and spheres. To investigate the influence of N on the temperature distribution, contour maps of temperature fields at different cross sections are depicted for random packings of spheres and Raschig rings with $N_{pv} = 6.1$ in Fig. 11.

As shown in Fig. 11, a considerable inhomogeneity in the temperature fields can be observed in wider packing structures as well. This behavior is more pronounced in packed beds with Raschig rings, where the presence of an internal hole in such pellets causes even a much sharper temperature gradient along the azimuthal direction at each crosscut. This thermal heterogeneity can be clearly discerned near the wall region, where the sharpest temperature gradients in both fluid and pellet phases exist. It is worth remarking that, the color maps of local temperatures at different cross section show an improved lateral heat dispersion in packings of Raschig rings and cylinders compared to spheres for similar N_{pv} values (see Figs. 10 and 11 for packings with $N_{pv} = 3.1$ and 6.1), which can be directly ascribed to the more tortuous flow fields.

4.2. Radial velocity and temperature profiles: The validity of azimuthal averaging

In our previous work [20], we noticed that the observed fluctuations in the local 3D axial velocity field are obscured by azimuthal-averaging

over the bed volume in low-N fixed beds of spheres and cylinders. We reported that the axially-and azimuthally-averaged velocity profile, $v_z(r)$, deviates by more than 500% from the local axial velocity values (mean relative error, MRE, expressed as percentage relative to the inlet velocity). Conceptually, a radially-varying axial velocity profile, $v_z(r)$, has been used to improve the classical plug-flow pseudo-homogenous models to account for the role of tortuous velocity fields. Here we take one step forward by casting light on the role of pellet-scale flow structures on the heat transfer and resulting 2D temperature profiles in a wall-heated fixed bed field with different pellet shapes. To that end, we assess how the deviations of the 3D velocity field from $v_z(r)$ carry over to deviations in the temperature field. Fig. 12a, c&e show the spread of the local temperature around the azimuthally-averaged temperature profile $T(r,z)$, at a typical bed cross section $z = 4.5d_p$, and $Re_p = 100$ in different packing structures. Fig. 12b, d&f show the corresponding spread of local axial velocity data around the azimuthally-averaged velocity profile $v_z(r,z)$, at the same bed cross section $z = 4.5d_p$, as well as the axially- and azimuthally-averaged velocity profile, $v_z(r)$. In all cases, velocities have been normalized with the inlet velocity.

These results show that the azimuthally-averaged axial velocity profile at a typical cross section, i.e. $v_z(r,z)$, slightly deviates from $v_z(r)$ in packings of spheres and cylinders, whilst a considerable deviation can be observed in Raschig rings packings. The significant deviations observed for $0.3 < (R_t - r)/d_{pv} < 0.6$ stem chiefly from the internal hole in Raschig rings pellets, and those observed around the bed center region can be ascribed to the presence of a channel along the axis of Raschig rings packing with $N_{pv} = 3.1$.

The results demonstrate that the deviations of $v_z(r)$ from $v_z(r,z)$ culminate in the positions of axial velocity peaks as exemplified in Figs. 12 and 15 for packing models of spheres and cylinders with $N_{pv} = 3.1$ and spheres and Raschig rings with $N_{pv} = 6.1$ at $Re_p = 100$, respectively. These deviations can be ascribed to the planar distribution of pellets at the cross section for which $v_z(r,z)$ is computed. Since the radial heterogeneity in packing structures culminates in narrower packed columns due to the restricting role of tube wall on particles ordering across the tube, a higher deviation of $v_z(r)$ from $v_z(r,z)$ is anticipated in very low N-beds as demonstrated with our results (see the axial velocity plots and graphs in Figs. 10 and 12 for packed column of rings with $N_{pv} = 3.1$).

The maximum deviation of the local axial velocity data in the cross section $z = 4.5d_p$ from $v_z(r)$ are $4.6v_0$, $5.11v_0$ and $3.9v_0$ (in terms of

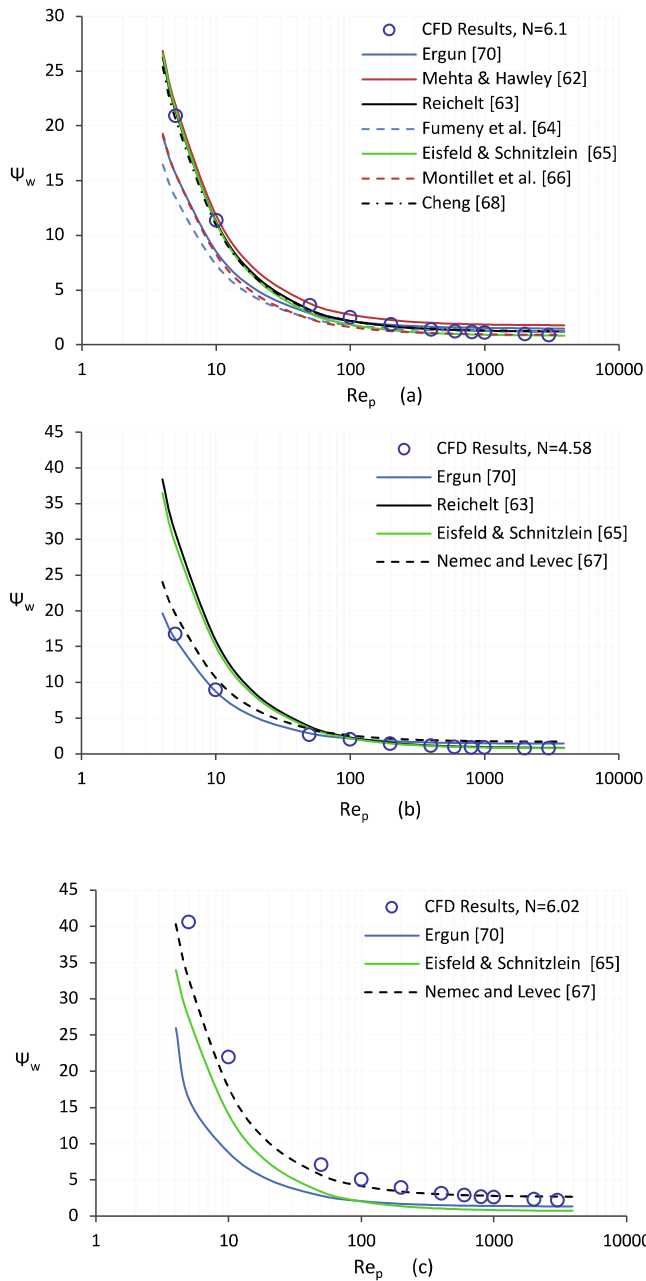


Fig. 8. Comparison between the computed pressure drops obtained from RBD-CFD simulations and empirical correlations for packings of (a) spheres with $N = 6.1$, (b) cylinders with $N = 4.58$ and (c) Raschig rings with $N = 6.02$.

Table 5

Deviation of the computed pressure drop as percent mean relative error from empirical correlations.

Dev. in MRE % from the empirical correlations	Packing of spheres with N:			Packing of cylinders with N:			Packing of Raschig rings with N:		
	3.1	4.1	6.1	2.29	3.55	4.58	3.06	4.05	6.02
Ergun [68]	39	28.7	25.6	49.5	30.8	25.6	28.9	67.5	75.2
Mehta & Hawley [60]	27.9	45.9	26.3	—	—	—	—	—	—
Reichelt [61]	11.2	26.7	11.7	19.5	30.6	37	—	—	—
Fumeny et al. [62]	85.2	21.6	27.4	—	—	—	—	—	—
Einfeld and Schnitzlein [63]	10.2	17.9	18.7	19.5	12.9	12.3	33.4	110.2	158.9
Montillet et al. [64]	73.8	18.2	28.5	—	—	—	—	—	—
Nemeec and Levec [65]	—	—	—	34.8	30.6	26.5	27.8	17.8	14.8
Cheng [66]	24.5	24.1	13.2	—	—	—	—	—	—

absolute errors) for packings of spheres, cylinders and rings with $N_{pv} = 3.1$, respectively. These maximum deviations occur within a region adjacent to the tube wall with thickness of $0.2d_{pv}$ for packings of spheres and cylinders with $N_{pv} = 3.1$, and at the position $(R_t - r)/d_{pv} = 0.5$ for Raschig ring packings with $N_{pv} = 3.1$. It is noteworthy that $v_z(r, z = 4.5d_p)$ reaches its maximum at the same position as the local void fraction, which possesses a high values of around 0.75 within a distance of $0.2d_{pv}$ from tube wall for all packing models and a high value of around 0.7 at a distance of $0.5d_{pv}$ from tube wall for the packing of Raschig rings. This can also be deduced from Fig. 13a wherein the variations of axial velocity deviations at different azimuthal positions for a typical cross section $z = 4.5d_p$ are plotted against the dimensionless distance from tube wall for all packing models with $N_{pv} = 3.1$ at $Re_p = 100$.

Similarly, the in-situ analysis of the temperature field (see Fig. 12a, c&e) demonstrate considerable deviations of the local temperature data obtained from different azimuthal positions at the typical bed cross sections $z = 4.5d_p$ and $8.5d_p$, from the azimuthally-averaged temperature profile, $T(r, z)$, for the packing models with $N_{pv} = 3.1$. These results demonstrate that (i) larger deviations of the local temperature data from $T(r, z)$ occur in the lower cross sections, where a higher thermal disequilibrium (difference between bulk temperatures of the individual phases) between the fluid and solid phases exists; (ii) the maximum deviations of the local temperature data from $T(r, z = 4.5d_p)$ are 56 K, 97 K and 103 K, observed at $(R_t - r)/d_{pv} = 0.1, 0.15$ and 0.43 for packings of spheres, cylinders and rings with $N_{pv} = 3.1$, respectively.

Fig. 13 shows maximum differences between maximum and minimum axial velocity (left figure) and temperature (right figure) computed at different azimuthal positions in the typical cross section $z = 4.5d_p$ as a function of dimensionless distance from the tube wall, for all packing models with $N_{pv} = 3.1$. The plot shows that the first peak of the deviations of local temperature data from $T(r, z)$ occurs in the region of sharpest temperature gradient and where the $v_z(r)$ and $v_z(r, z)$ profiles have their first maximum, i.e. within a distance of $0.15d_{pv}$ from the tube wall. In fact, local void fraction in this region is higher than 0.75,

Table 6

Empirical correlations proposed for Nu.

Author	Nusselt Number (Nu and Nu_{fs})	Application range	Re_p
Gupta et al. [69]	$Nu = \frac{Pr^{1/3}}{\epsilon} Re_p (0.0108 + \frac{0.929}{Re_p^{0.58} - 0.483})$	$0.26 < \epsilon < 0.78$	$10 \sim 10,000$
Gunn [70]	$Nu = (7 - 10\epsilon + 5\epsilon^2)(1 + 0.7Re_p^{0.2}Pr^{1/3}) + (1.33 - 2.4\epsilon + 1.2\epsilon^2)(Re_p^{0.7}Pr^{1/3})$	$0.35 < \epsilon < 1$	$20 \sim 10^5$
Wakao et al. [71]	$Nu = 2 + 1.1Re_p^{0.6}Pr^{1/3}$	$2 < N < 107.6$	$15 \sim 500$
Sun et al. [72]	$Nu = (-0.46 + 1.77\epsilon + 0.69\epsilon^2)/\epsilon^3 + (1.37 - 2.4\epsilon + 1.2\epsilon^2)Re_p^{0.7}Pr^{1/3}$	$0.5 \leq \epsilon < 1$	$1 \sim 100$
Singhal et al. [28]	$Nu = 2.67 + 0.53Re_p^{0.77}Pr^{0.53}$	$0.35 < \epsilon < 0.37$	$9 \sim 180$

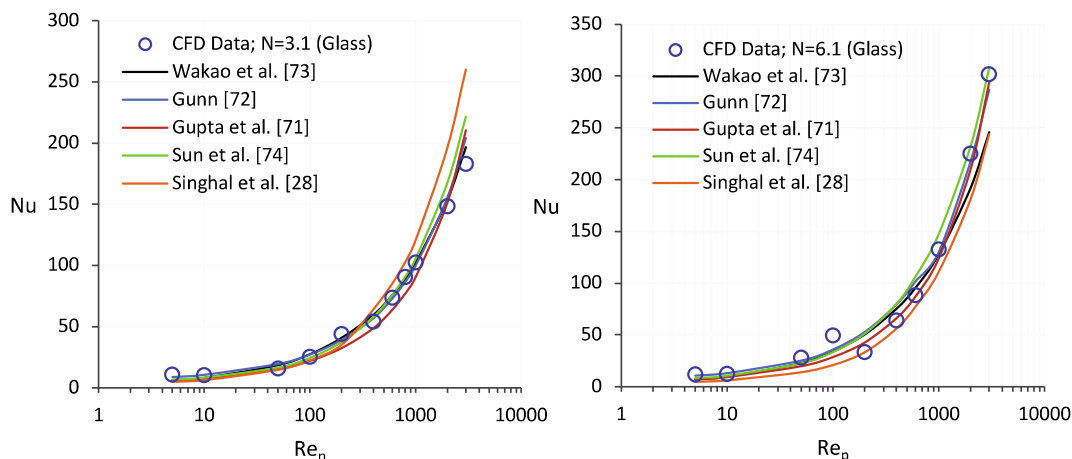


Fig. 9. Comparison between computed fluid-to-solid Nusselt number for glass particles and published correlations for packing models of spheres; (a) $N = 3.1$, (b) $N = 6.1$.

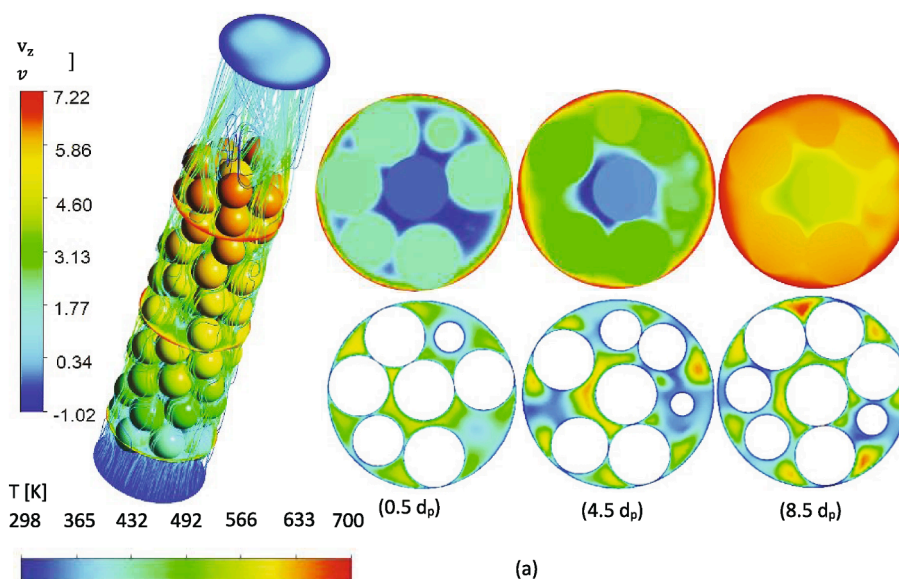


Fig. 10. Contour plots of axial velocity normalized by the inlet velocity and temperature fields at different cross sections at axial positions $0.5d_p$, $4.5d_p$, $8.5d_p$, for packings of alumina pellets; (a) spheres, (b) cylinders and (c) Raschig rings, with $N_{pv} = 3.1$ at $Re_p = 100$. The flow streamlines together with the inlet and outlet of the reactor tube are colored by the axial velocity.

resulting in a large temperature difference between the stagnant phase and the fluid phase. Besides, as shown in Fig. 13a, the first peak of the deviations of local axial velocity data from $v_z(r,z)$ occurs slightly further at a distance of $0.2d_{pv}$ from the tube wall.

Fig. 12 and Fig. 13b show that another peak of deviation of local temperature from $T(r, z = 4.5d_p$ and $8.5d_p)$ takes place at a distance of $1d_{pv}$ from the tube wall for packings of spheres and cylinders and Raschig rings. The Raschig rings also have a peak of deviation at a distance of approximately $0.5d_{pv}$ from the tube wall (viz. the second peak of $v_z(r)$, $v_z(r,z)$ and $\epsilon(r)$ occurs at the same distance from the tube wall for packings of Raschig rings due to the axial hole within the rings).

According to the results shown in Fig. 12 and Fig. 13b, minimum deviations of local temperature data from $T(r, z = 4.5d_p$ and $8.5d_p)$ occur at an approximate wall distance of $0.5d_{pv}$ and $0.6d_{pv}$ for packings of spheres and cylinders, respectively, and $0.15d_{pv}$ and $0.75d_{pv}$ for packings of Raschig rings, all of which coincide with the positions of minima in the radial porosity and azimuthally-averaged axial velocity profiles. The local porosity in these regions decrease to even lower than 0.3 for

packings of spheres and cylinder, implicating the major contribution of pellet phase temperature in the circumferentially-averaged temperature and axial velocity. In addition, since the volume fraction of backflow fields escalates in such regions (see [20,74]), the deviation of $T(r,z)$ from the local data can significantly decrease, reaching in its minima as observed in the plots of ΔT versus $(R_t-r)/d_{pv}$. Similar justifications can be offered to interpret the correlation between the peaks in the radial porosity profile and those in the plot of $\Delta v_z/v_0$ versus $(R_t-r)/d_{pv}$. These results show where we may anticipate maximum and minimum deviations of azimuthally-averaged temperature profiles from local data inside a reactor.

Next, we investigate the influence of inlet flow velocity on the amount of local deviations from the azimuthally-averaged temperature profiles. Basically, the deviations of $T(r,z)$ from the local data originate from the thermal disequilibrium between the individual phases. This implies that larger deviations should emerge (i) at lower cross sections (shown in Fig. 12a, c&e), (ii) at higher flow conditions, i.e. higher inlet velocity, v_0 . Fig. 14a shows deviations of the local temperature with $T(r,$

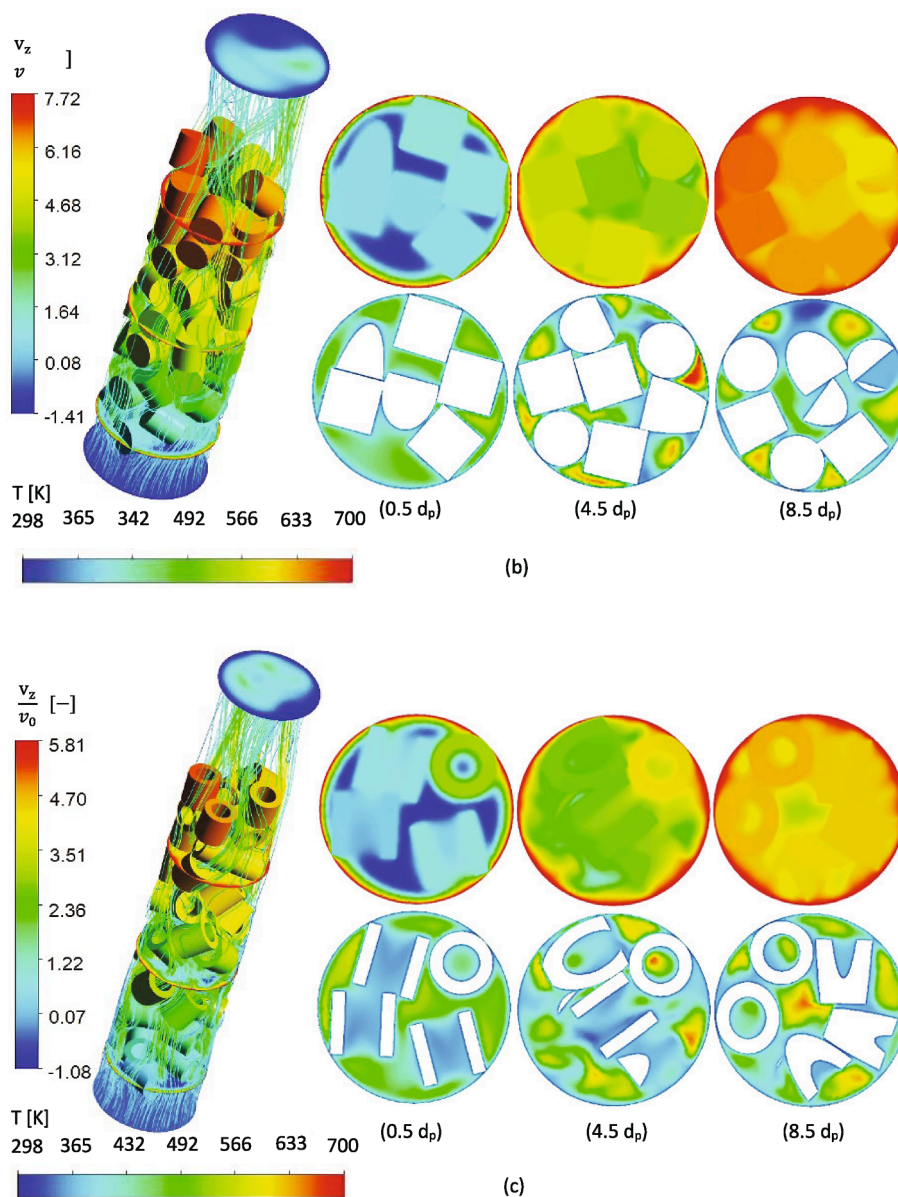


Fig. 10. (continued).

$z = 4.5d_p$) and Fig. 14b shows the differences between maximum and minimum temperature values at $z = 4.5d_p$ at $Re_p = 100$ and 200 , for a packing of cylinders with $N_{pv} = 3.1$. The local temperature differences ΔT reach their maxima at approximately $(R-r)/d_{pv} = 0.15$ and 1 , with larger differences occurring for $Re_p = 200$ than for $Re_p = 100$. This can be attributed to the large local porosity at these positions which lead to lower fluid bulk temperature in the void spaces for $Re_p = 200$ compared to $Re_p = 100$, and consequently a higher temperature difference between two phases.

Of course the simulated results also depend on the thermal conductivity of the solid (catalyst pellet) material. Fig. 14c-d shows local temperature deviations at cross section $z = 4.5d_p$ for packed columns of alumina and glass cylinders with $N_{pv} = 3.1$ at $Re_p = 100$. Although the average temperature profiles between the two different materials are quite different (Fig. 14c), the differences between local maximum and minimum temperature are quite comparable (Fig. 14d). This could have been expected because the local heterogeneities in the temperature field are primarily driven by local heterogeneities in the flow field.

The same analysis has been conducted for wider beds containing Raschig rings and spheres with $N_{pv} = 6.1$, see Fig. 15. In general, the

results demonstrate slightly higher deviations for $T(r, z = 4.5d_p)$ from the local temperature data in wider beds at similar Re_p . This can be explained by the lower radial and azimuthal heat transfer rates in larger N -beds at the same flow and thermal boundary conditions, leading to a higher temperature difference between the fluid and pellet phases, and consequently larger deviations of the local temperature from the azimuthally-averaged temperature profile. For packings of spheres and Raschig rings with $N_{pv} = 6.1$, the maximum deviations of $T(r, z = 4.5d_p)$ from the local temperature are 65 K and 113 K, which occur at $(R-r)/d_{pv} = 0.15$ and 1 (see Fig. 15a, b&e). It seems that contrary to the same packings with $N_{pv} = 3.1$, wherein maximum deviations of the azimuthally-averaged temperature profile from the local data generally occur at a distance of $0.2d_{pv}$ from the tube wall, maximum deviations in wider packing structures take place at a distance of $1d_{pv}$ from the tube wall. Similar results were found for packing models with $N_{pv} = 4.1$ which are not addressed here for the sake of brevity.

Furthermore, the results presented in Fig. 15c, d&f suggest that the deviations of the local axial velocity data from $v_z(r)$ and $v_z(r, z = 4.5d_p)$ are much larger than those obtained for the same packing models with $N_{pv} = 3.1$ at similar Re_p . This can be explained by the fact that the local

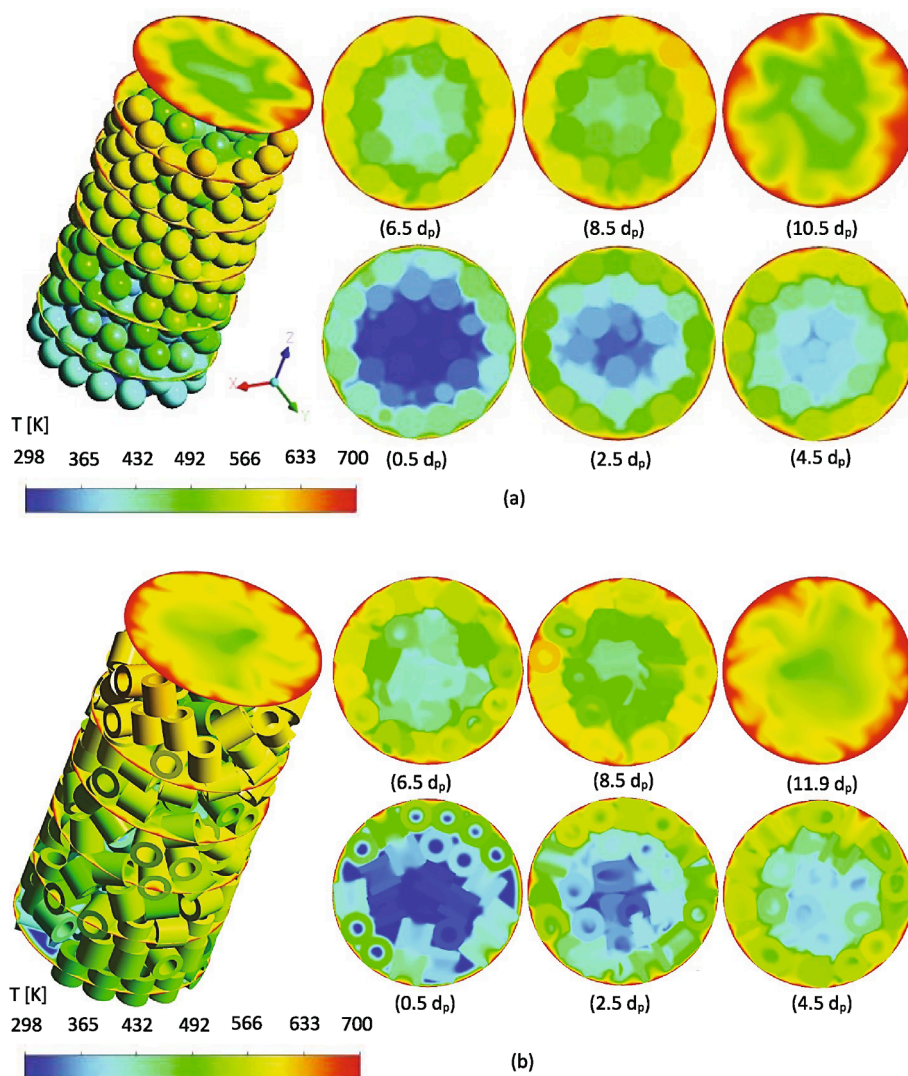


Fig. 11. Contour plots of the temperature field on the surface of pellets and at different cross sections at axial positions $0.5d_p$, $2.5d_p$, $4.5d_p$, $6.5d_p$, $8.5d_p$ and $+0.5d_p$ behind the packing section, for packings of alumina spheres (a) and Raschig rings (b) with $N_{pv} = 6.1$ at $Re_p = 100$.

void fraction decreases with increasing N , thus leading to a higher local axial velocity inside the larger- N packings at similar flow conditions. For the packings of spheres and Raschig rings with $N_{pv} = 6.1$, the maximum deviations of $v_z(r)$ from the local axial velocity data (for cross section $z = 4.5d_p$) are $7.31v_0$ and $7.6v_0$, which occur within a distance of $0.2d_{pv}$ from the tube wall.

Overall, Figs. 12-15 illustrate that the azimuthally-averaged temperature profiles in packed beds of cylinders and Raschig rings demonstrate a much smoother pattern along the tube radius than spheres. Similarly, smoother radial temperature profiles in the pellet and solid phases can also be observed in Fig. 16, indicating more efficient lateral heat dispersion provided by such packings. This can also be elucidated by a very steep “hump” or “shoulder” observed in $T(r,z)$ in packings of spheres compared to cylinders and rings, which usually occurs at an approximate distance of $0.8d_{pv}$ to $1d_{pv}$ from the tube wall in all packing models. This steep hump emerges due to a very sharp temperature gradient at the surface of the pellets adjacent to the tube wall and seems to be much smoother in the packings of cylinders and rings. It is worth noting that these features, i.e. the presence of a hump or shoulder in the radial temperature profile, have been previously addressed by several researchers, e.g. [5,19,25,76].

Fig. 16 demonstrates the significant role of the pellet’s thermal conductivity on the azimuthally-averaged temperature profile in

individual phases. This can be interpreted by approximating a fixed bed arrangement as a 2D quasi-homogenous medium, wherein the heat transfer is characterized by effective lumped parameters. In such a system, the presence of a low temperature gradient field over a large fraction of the tube radius, say $0.2 < (R-r)/d_{pv} < 0.8d_{pv}$, is associated with a very large effective radial thermal conductivity, k_{er} . Such a region emerges due to the higher contribution of the conductivity through the catalyst phase, particularly for alumina pellets (see Fig. 16b). According to these results, the effective radial thermal conductivity, i.e. k_{er} , should be a function not only of Re_p , but also of N and pellet thermal conductivity.

The behavior of the azimuthally-averaged temperature profiles suggests that there are two different thermal regions as a function of distance to the tube wall: a near wall region with a thickness of around $0.2d_p$, where a large temperature gradient exists, and a core region. Such a differentiation is in agreement with experimental observations by Froment and coworkers [77,78] and, more recently, by Dong et al. [6]. It is worth reiterating that the axial velocity peaks appear in the same region, i.e. within a distance of around $0.2d_p$ from the tube wall, for all packing models. Since the local porosity at the location of axial velocity peaks in the wall region is larger than 0.75, the contribution of the fluid phase temperature is considerable in the azimuthally-averaged temperature profile. This observation can also explain the influence of the

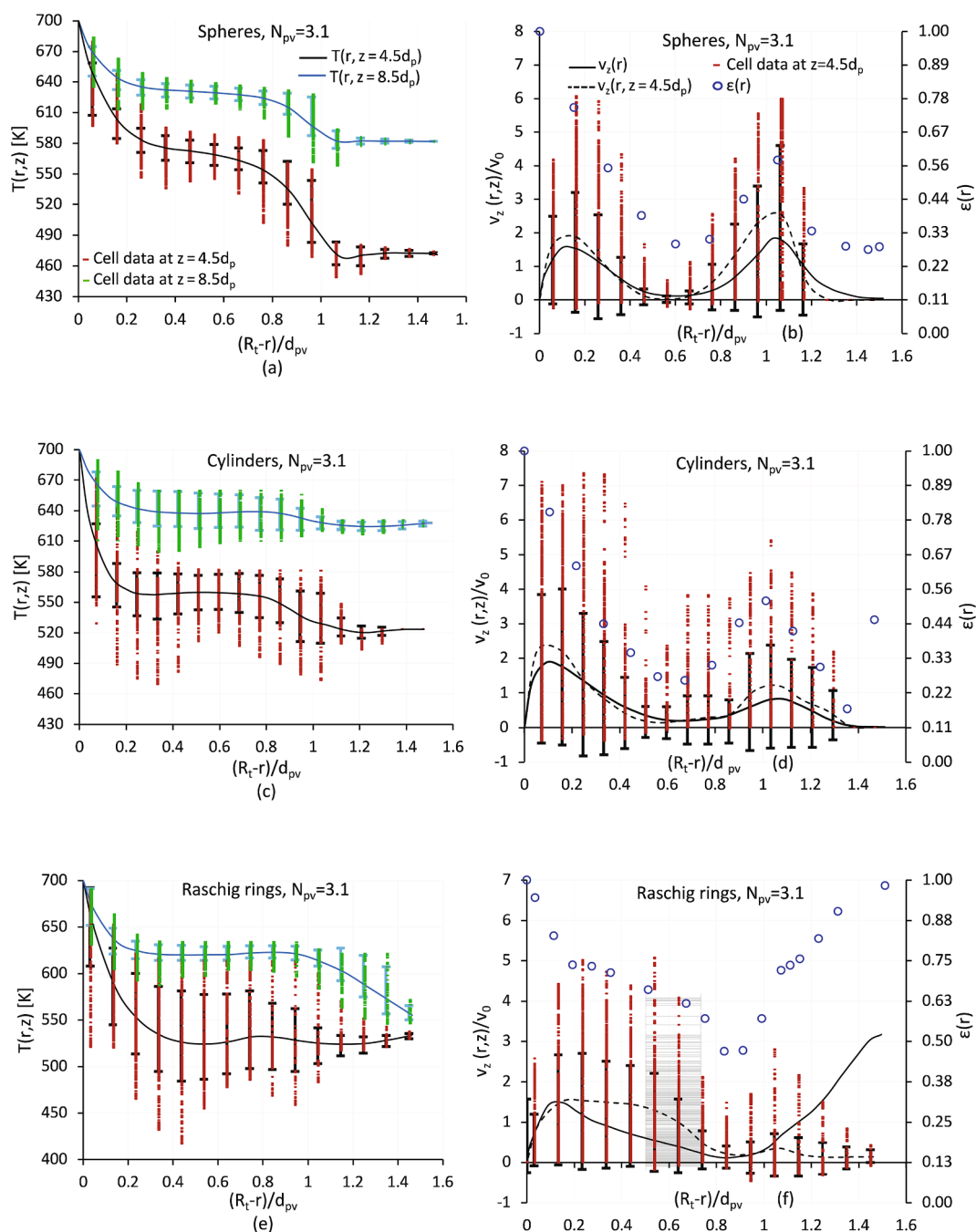


Fig. 12. Left hand side graphs: comparison between the azimuthally-averaged temperature profile (solid lines) and the local temperature (symbols, standard deviations indicated by bars) at cross sections $z = 4.5d_p$ and $z = 8.5d_p$ for packed columns of alumina pellets with $N_{pv} = 3.1$ at $Re_p = 100$. Right hand side graphs: comparison between the (axially- and) azimuthally-averaged axial velocity profile (solid lines) and the local axial velocity (red symbols, standard deviations indicated by black bars), normalized by the inlet velocity, at cross section $z = 4.5d_p$ in random packings with $N_{pv} = 3.1$ at $Re_p = 100$. The axially- and azimuthally averaged porosity distribution is shown by blue circles. (For interpretation of the references to color in this figure legend, the reader is referred to the web version of this article.)

wall-channeling phenomenon on the radial temperature profile.

Fig. 17 illustrates the evolution of 2D (azimuthally-averaged) temperature profiles in packings of alumina spheres, cylinders and Raschig rings with $N_{pv} = 3.1$ along the tube axis for $Re_p = 100$.

As shown in Fig. 17, the humps appear to be a little smoother in packings of cylinders and Raschig rings, evidencing the significant role of pellet shape in radial heat transfer. Furthermore, the position of the observed hump does not change along the bed height in all packings, although it seems to be smoothed or even disappears as the local temperature in the fluid and the pellet phases approach equilibrium

conditions. Moreover, the CFD results demonstrate independence of the radial position of the observed humps with changing Re_p (not shown).

To investigate the influence of N on the radial temperature profiles, the azimuthally-averaged temperature profile for alumina packings of spheres, cylinders and rings with different N at typical cross section $z = 6d_p$ and $Re_p = 100$ is depicted in Fig. 18.

Fig. 18 and also Fig. 15a,b reveal the presence of a second hump in wider beds at a distance of around $1.6d_{pv}$ to $2d_{pv}$ from the tube wall, which is however much smoother than the first hump. It can also be deduced that the presence of a hole in the middle of the packing

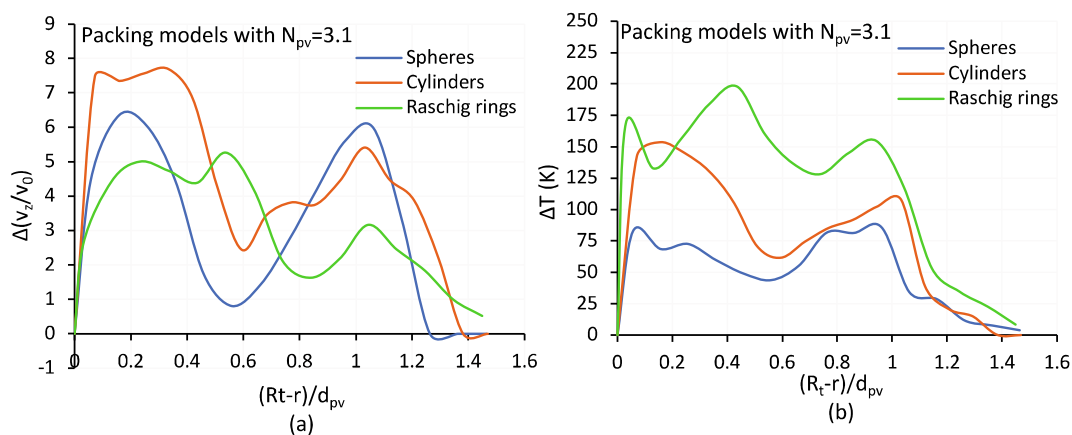


Fig. 13. Pronounced difference between maximum and minimum local normalized velocity (left) and local temperature (right) from azimuthally averaged values for $z = 4.d_p$ for packing models of spheres, cylinders and Raschig rings with $N_{pv} = 3.1$ at $Re_p = 100$.

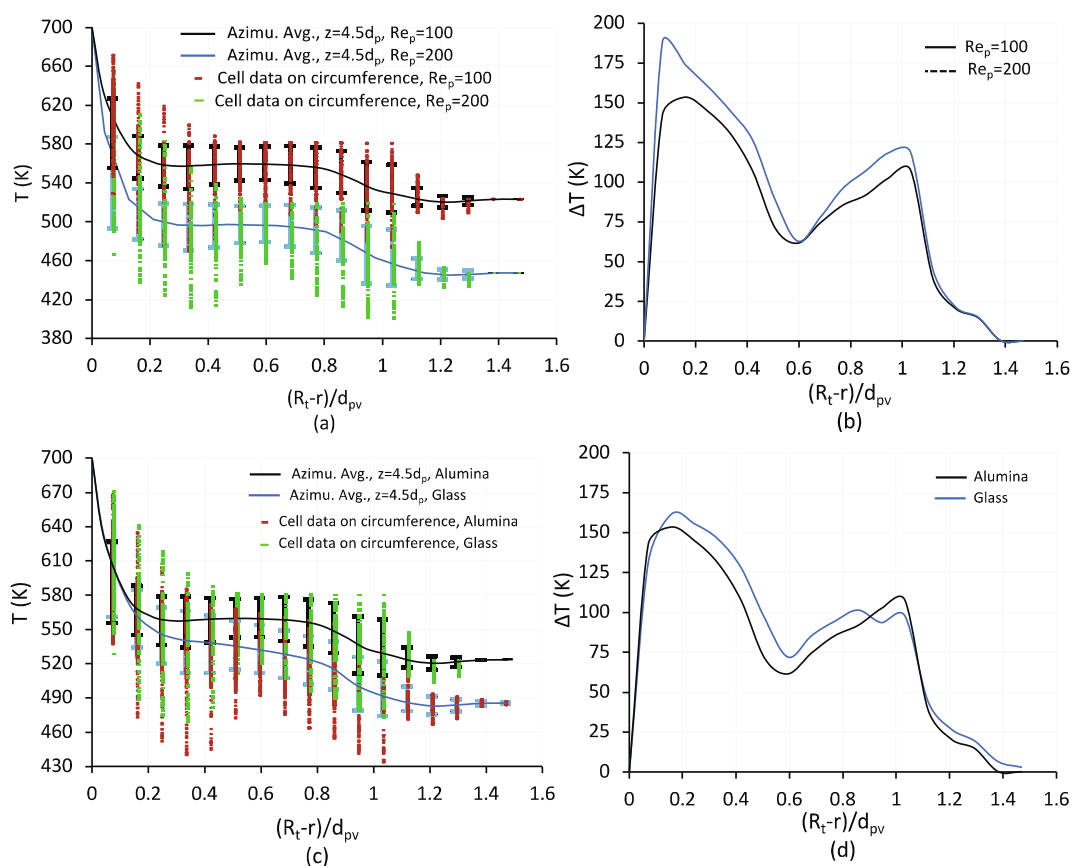


Fig. 14. Comparison between the local temperature data and the azimuthally-averaged temperature profile at $z = 4.5d_p$ for a packed bed of cylinders with $N_{pv} = 3.1$ (a) for alumina pellets at $Re_p = 100$ and 200 , (c) for alumina and glass pellets at $Re_p = 100$. Standard deviations in the local data are indicated by bars. Differences between the maximum and minimum temperature values obtained at different azimuthal positions at $z = 4.5d_p$ (b) at $Re_p = 100$ and 200 for alumina pellets, (d) for alumina and glass pellets at $Re_p = 100$.

structures of spheres and cylinders with $N_{pv} \approx 4$, leads to poorer radial heat transfer compared to the packing of Raschig rings with $N_{pv} = 4.1$ (see Fig. 18). Furthermore, Fig. 18 shows much smoother temperature profiles in packings of cylinders and Raschig rings, even for wider tubes.

4.3. Validity of k_{er} - h_w heat transfer model

One of the mostly-used models for predicting heat transfer rate from reactor wall to catalyst bed in heterogeneous catalytic flow reactors is

undoubtedly the 2D axial dispersive plug flow heat transfer model (2D-ADPFM), i.e. the well-known $k_{er} - h_w$ model [12,22,79–81]. In fact this model presents a few features of the reactor thermal behavior, which are suitable for fast and repetitive computations for *a priori* design, adaptive control, sensitivity analysis, etc. However, due to the inherent simplicity of the $k_{er} - h_w$ model, i.e. symmetry, regularity, and homogeneity of packing topology, plug flow idealization and the use of lumped heat transfer parameters, the limitations of this approach have been the subject of active research for more than 50 years [11,12,14–16,22,82].

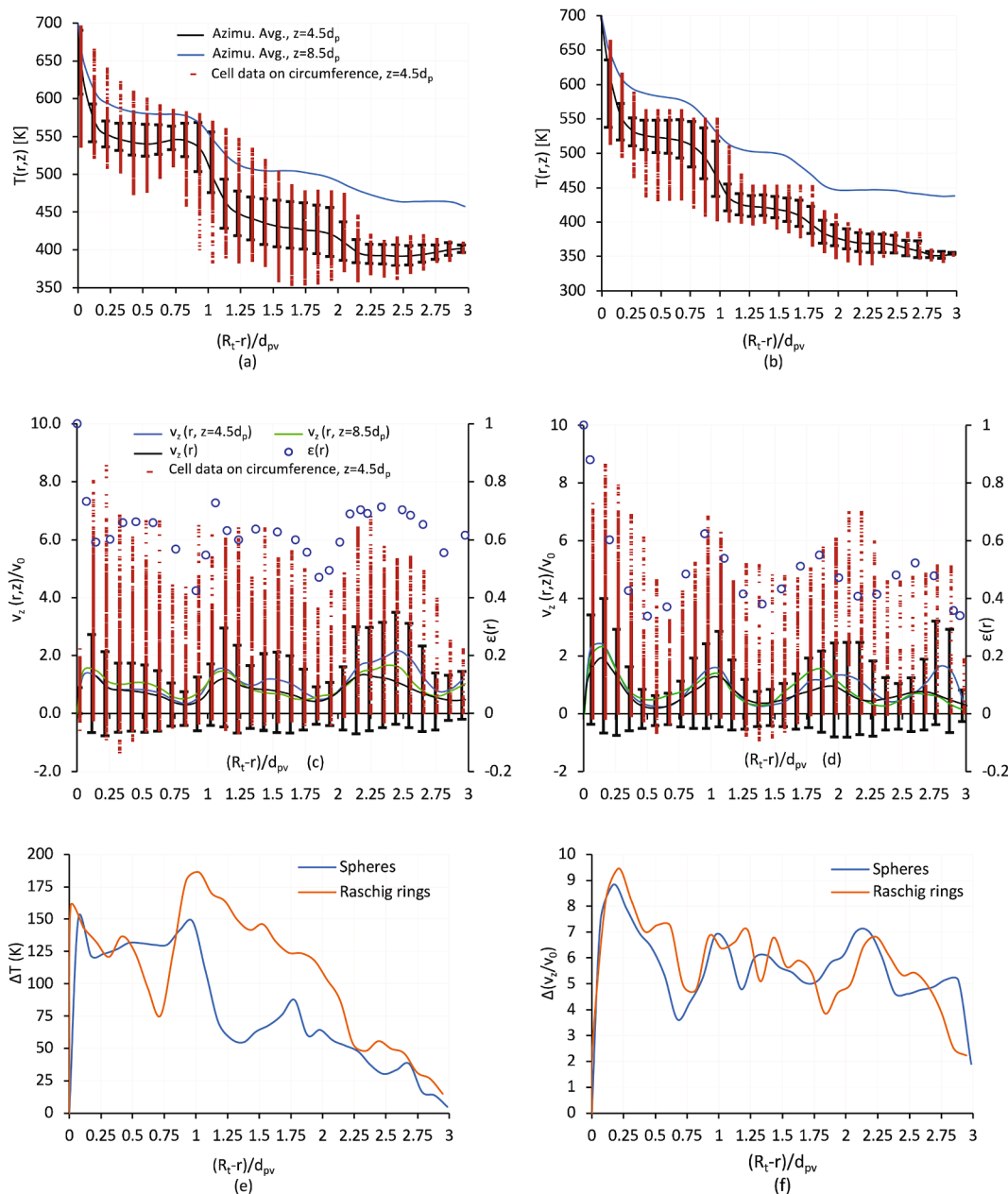


Fig. 15. Comparison between the azimuthally-averaged temperature and normalized axial velocity profiles with the local data sampled from different azimuthal positions at cross section $z = 4.5d_p$ in packings of (a,c) alumina Raschig rings (b,d) alumina spheres with $N_{pv} = 6.1$ at $Re_p = 100$. Standard deviations of local data are indicated by bars. Comparisons between the variations of (e) temperature ranges and (f) axial velocity ranges at cross section $z = 4.5d_p$ in the same packings and for the same flow and thermal boundary conditions.

Here, we apply the concept of a numerical experiment based on the particle-resolved CFD simulation results to investigate the validity of radial temperature profiles obtained from the $k_{er} - h_w$ model. To this end, the effective radial thermal conductivity, k_{er} , and the apparent wall heat transfer coefficient, h_w , were computed by solving the inverse problem using an in-house code in Matlab based on a nonlinear least-squares technique. For this, the numerical results of heat transfer are fed to the model in which the effective axial thermal conductivity is computed using Zehner and Schlünder [83] correlation, assuming $Pe_{af(\infty)} = 2$, and the best-fitted values of k_{er} and h_w are used in the model to compare the radial temperature profile with the azimuthally-average temperature profile obtained in our RBD-CFD simulations. Fig. 19 shows the comparison between the azimuthally-averaged temperature profiles obtained from the RBD-CFD heat transfer results and the radial temperature profiles predicted by the 2D-ADPF heat transfer model

based on the optimum values of k_{er} and h_w for packings of Raschig rings with $N_{pv} = 3.1$ and 6.1 at different cross sections.

As illustrated in Fig. 19, the radial temperature profile predicted by 2D-ADPF heat transfer model cannot anticipate the hump shape in the azimuthally-averaged temperature profile due to the fact that the model basically presumes no thermal resistance between fluid and pellet phases. Therefore, the 2D-ADPF heat transfer model is unable to reflect the role of thermal disequilibrium between individual phases along both the tube radius and reactor depth. A better fit can be foreseen at higher bed cross sections where thermal equilibrium has (almost) been reached between both phases, and thus the assumption of no thermal resistance between the two phases is legitimate.

Nevertheless, large deviations between the azimuthally-averaged temperature profile and the local temperature data can also be notified here. Furthermore, it can also be deduced that these deviations are

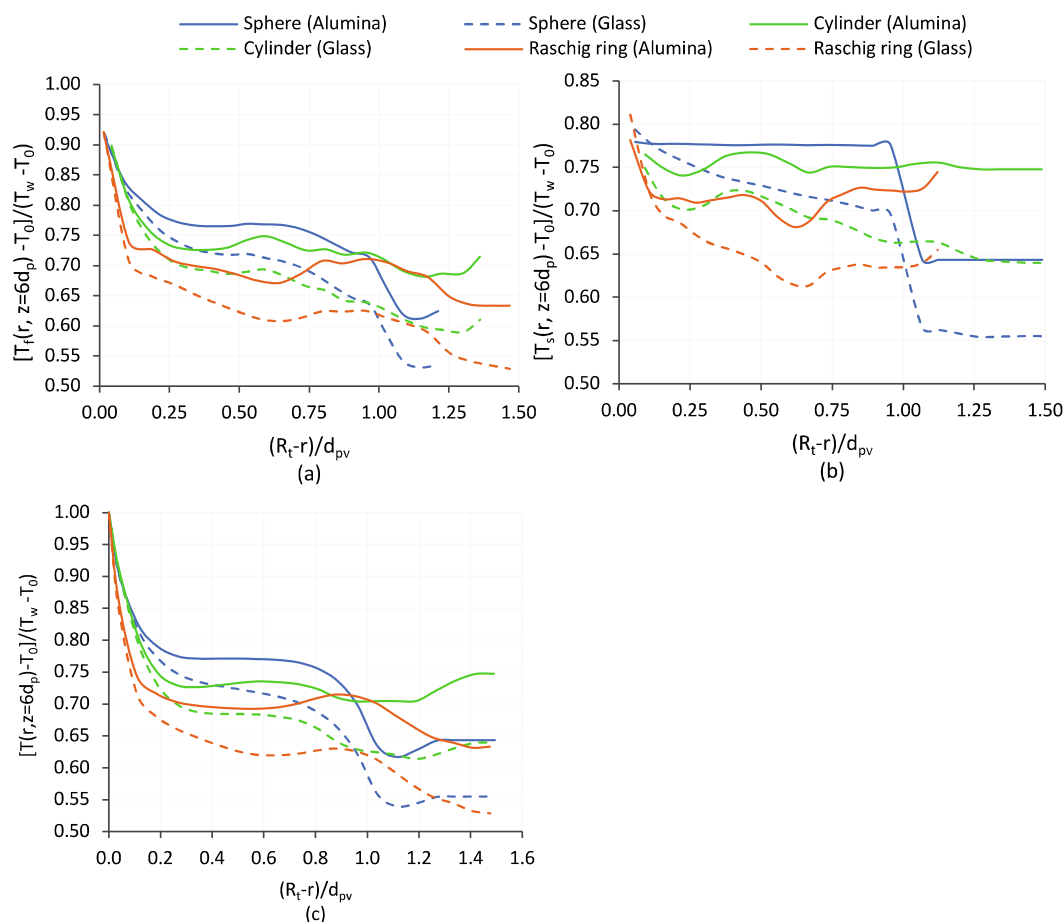


Fig. 16. Azimuthally-averaged temperature profile for packings of spheres, cylinders and Raschig rings with $N_{pv} = 3.1$, at the packing depth $z = 6d_p$ for glass and alumina pellets at $Re_p = 100$; (a) azimuthally-averaged fluid phase temperature, (b) azimuthally-averaged pellet phase temperature, (c) azimuthally-averaged temperature of all phases.

much larger for the radial temperature profile obtained from 2D-ADPF heat transfer model as it further underestimate the azimuthally-averaged temperature profile at the position of the hump (see Fig. 19), i.e. at the approximate distance of $1d_{pv}$ from the tube wall, where one of the largest deviations of the azimuthally-averaged temperature profile from the local temperature data was found (see Fig. 15e&18b).

It is noteworthy that the condition of thermal disequilibrium between two phases is much more substantial when chemical reactions with large heat effects occur at the pellet scale. Therefore, even larger deviations of the local temperatures from the radial temperature profiles obtained from the 2D-ADPF model can be anticipated in such cases, even when the effective heat transfer parameters are precisely introduced. To provide optimum reactor performance for such reaction cases, the operating conditions usually need to be kept as close as possible to the run-away zone. So the question is, with the observed significant deviations of the local data from 2D temperature profiles, how accurate a 2D-ADPF heat transfer model can predict the heat transport properties and the position of the hot-spot to prevent run-away and deactivation of the catalyst?

Apart from the observed deviations of radial (averaged) temperature profile from the local data, our results in Fig. 19 demonstrate that using the concept of numerical experiment to compute the best-fitted values of k_{er} and h_w can tremendously improve the accuracy of pseudo-homogenous heat transfer models as the available predictive correlations for the effective heat transfer coefficients shows a large scattering over Re_p [11–14]. Furthermore, it is reiterated that since the values of these parameters are computed per cross section along the reactor, the length-dependency of k_{er} and h_w has already been considered in the best-

fitted values.

Overall, the findings of this research suggests the inadequacy of both the azimuthal averaging of 3D velocity fields and the radial temperature profiles obtained from the 2D-ADPF heat transfer model for accurate prediction of heat transfer from reactor walls to a particulate bed in narrow-tube heterogeneous catalytic flow reactors with large heat effects.

5. Conclusion

Discrete-pellet CFD simulations of the hydrodynamics and lateral heat transfer in fixed beds of spheres, equilateral solid cylinder and Raschig rings were performed for laminar, transient and fully turbulent flow regimes. CFD results were validated by comparing the numerical results to often-cited empirical correlations for pressure drop and fluid-to-solid heat transfer coefficient. Overall, comparison shows good agreement, evidencing the merit of the empirical correlations by Einfeld & Schnitzlein [63] for packed columns of spheres and cylinders and Nemeč and Levec [65] for packed columns of rings for the use in engineering design calculations of narrow-tube fixed bed systems. Similarly, validation results demonstrate a remarkable agreements with the empirical correlations proposed by Gunn [70] and Sun et al. [72] for fluid-to-solid heat transfer Nusselt number.

Overall, the CFD simulations demonstrate very large inhomogeneity in local velocity and temperature fields which originate from the substantial topological heterogeneity inherent in low- N packing structures. Results point out the inadequacy of 120° wall-segment packing models for CFD analysis of flow and heat transfer in a full narrow-tube fixed

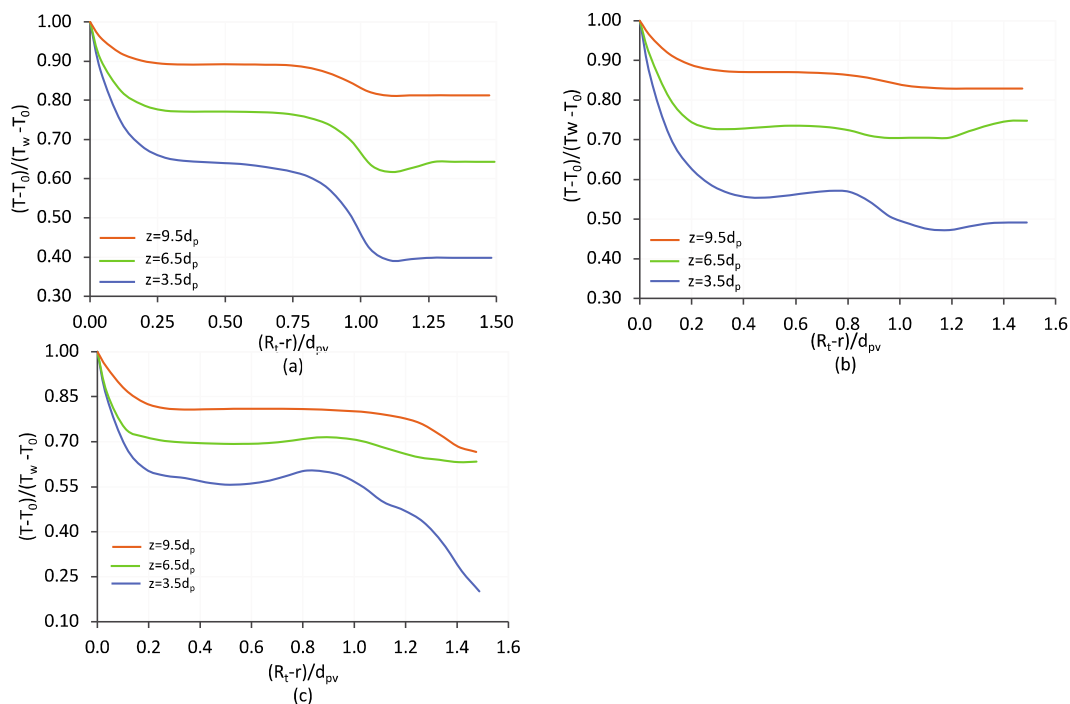


Fig. 17. Azimuthally-averaged temperature profiles for packings of alumina pellets with $N_{pv} = 3.1$, at the packing depth $z = 3.5d_p$, $6d_p$ and $9.5d_p$ at $Re_p = 100$; (a) spheres, (b) cylinders, and (c) Raschig rings.

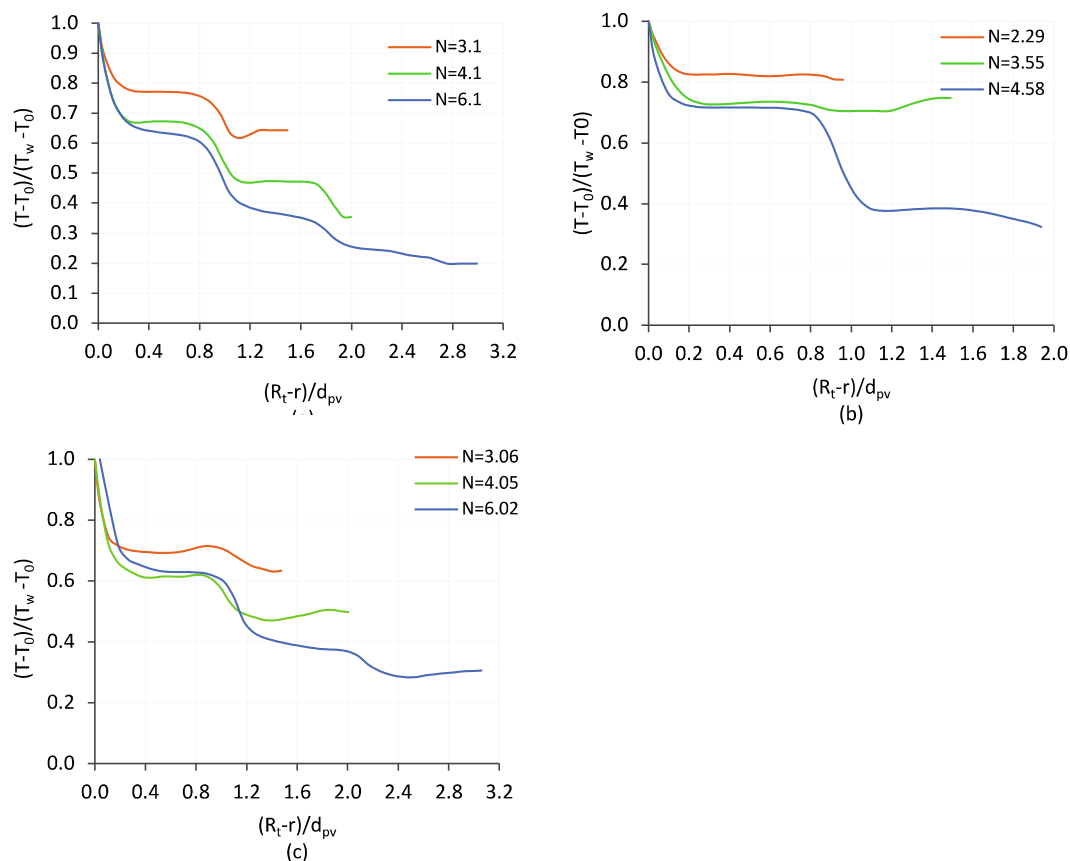


Fig. 18. Azimuthally-averaged temperature profiles for packings of alumina pellets with different N at cross section $z = 6d_p$ at $Re_p = 100$; (a) spheres, (b) cylinders, and (c) Raschig rings.

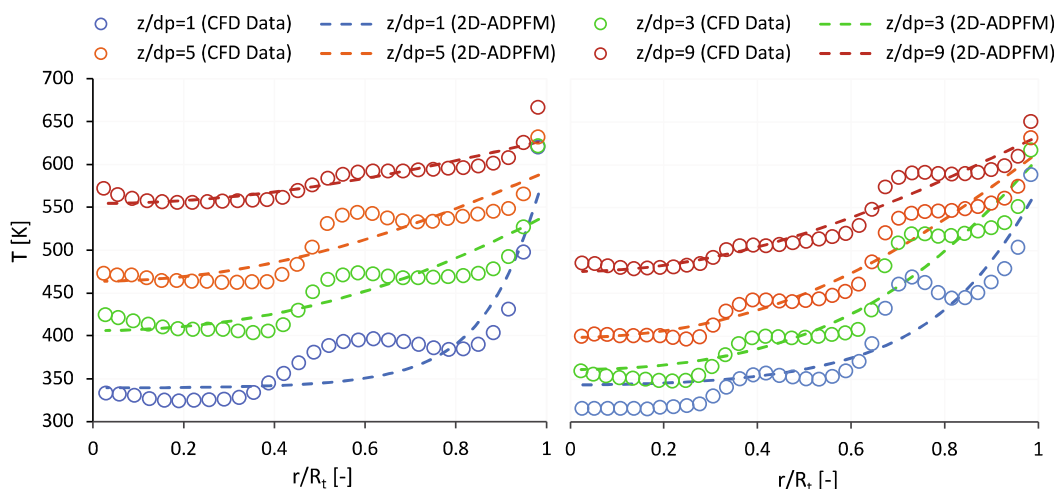


Fig. 19. Comparison between the azimuthally-averaged temperature profiles obtained from RBD-CFD results and the radial temperature profile predicted by the 2D-ADPF heat transfer model at cross sections $z = 1d_p, 3d_p, 5d_p$ and $9d_p$ in random packings of alumina Raschig rings with (a) $N = 4.05$ and (b) 6.02 , at $Re_p = 100$.

beds as the role of azimuthal heterogeneity of the bed structure is omitted in two-thirds of the bed cross section. The contour maps reveal completely different local velocity and temperature fields in random packings of cylinders and Raschig rings compared to in random packings of spheres, where (i) sharp edges of such pellets impose stronger curvatures of the flow streamlines along the packing, thereby improving the local heat dispersion at the pellet scale, and (ii) the presence of an internal hole in Raschig rings can tremendously affect the local velocity field according to the orientation of the pellets within the structure.

A detailed analysis on the validity of azimuthal averaging of 3D velocity and temperature fields in low- N fixed beds has brought some conclusions. The scattering of local 3D axial velocity and temperature data are totally concealed and, thus, omitted by azimuthal-averaging of 3D temperature and velocity fields over the bed volume, leading to more than $150\text{ }^\circ\text{C}$ deviation from local temperature data. Such deviations can substantiate that relying on radial (averaged) temperature profiles for feed-forward control of temperature in tubular catalytic flow reactors with large heat effects are in danger of misprediction of hotspots in each and every cross-section along the reactor, leading to excessive deactivation of catalysts and operation in localized run-away thermal zones.

Furthermore, these deviations between local velocity and the azimuthally-averaged velocity field are transmitted to the temperature field. This was evidenced by the coincidence of positions, i.e. the distance from tube wall, with largest deviations of $T(r,z)$ from local temperature data and $v_z(r)$ from local axial velocity data, viz. the positions of peaks in the plots depicting ΔT vs. $(R_t - r)/d_{pv}$ and $\Delta(v_z/v_0)$ vs. $(R_t - r)/d_{pv}$. For faster flow conditions, and in the beginning part of a packing section, a larger deviation of $T(r,z)$ from local temperature data is observed, with a similar thermal boundary condition. Our results show that the deviations become damped from the near-wall region (with a thickness of $1d_{pv}$) towards the bed core region, particularly for larger N -packing where a longer packing depth is necessary to reach thermal equilibrium.

The results of azimuthally-averaged temperature profiles at different cross sections show a smoother radial temperature profile for packings of cylinders and Raschig rings, compared to spheres, offering an improved radial heat dispersion in such packings.

Lastly, we found that the radial temperature profile obtained from a 2D-ADPF heat transfer model cannot predict the presence of a hump in the azimuthally-averaged temperature profile obtained from CFD results, which is ascribed to the assumption of thermal equilibrium between individual phases.

Declaration of Competing Interest

The authors declare that they have no known competing financial interests or personal relationships that could have appeared to influence the work reported in this paper.

References

- [1] F. Trifirò, R.K. Grasselli, How the Yield of Maleic Anhydride in n-Butane Oxidation, Using VPO Catalysts, was Improved Over the Years, *Top. Catal.* 57 (14-16) (2014) 1188–1195, <https://doi.org/10.1007/s11244-014-0285-5>.
- [2] E.H. Stitt, Reactor technology for syngas and hydrogen, in: *Sustain. Strateg. Upgrad. Nat. Gas Fundam. Challenges, Oppor.*, Springer, 2005: pp. 185–216.
- [3] A.I. Anastasov, A study of the influence of the operating parameters on the temperature of the hot spot in a fixed bed reactor, *Chem. Eng. J.* 86 (3) (2002) 287–297, [https://doi.org/10.1016/S1385-8947\(01\)00178-4](https://doi.org/10.1016/S1385-8947(01)00178-4).
- [4] A.G. Dixon, M. Nijemeisland, E.H. Stitt, Packed tubular reactor modeling and catalyst design using computational fluid dynamics, *Adv. Chem. Eng.* 31 (2006) 307–389, [https://doi.org/10.1016/S0065-2377\(06\)31005-8](https://doi.org/10.1016/S0065-2377(06)31005-8).
- [5] P. Magnico, Pore-scale simulations of unsteady flow and heat transfer in tubular fixed beds, *AIChE J.* 55 (4) (2009) 849–867, <https://doi.org/10.1002/aic.11806>.
- [6] Y. Dong, B. Sosna, O. Korup, F. Rosowski, R. Horn, Investigation of radial heat transfer in a fixed-bed reactor: CFD simulations and profile measurements, *Chem. Eng. J.* 317 (2017) 204–214, <https://doi.org/10.1016/j.ces.2017.02.063>.
- [7] E.I. Smirnov, A.V. Muzykantov, V.A. Kuzmin, A.E. Kronberg, I.A. Zolotarskii, Radial heat transfer in packed beds of spheres, cylinders and Raschig rings, *Chem. Eng. J.* 91 (2-3) (2003) 243–248, [https://doi.org/10.1016/S1385-8947\(02\)00160-2](https://doi.org/10.1016/S1385-8947(02)00160-2).
- [8] S.J.P. Romkes, F.M. Dautzenberg, C.M. van den Bleek, H.P.A. Calis, CFD modelling and experimental validation of particle-to-fluid mass and heat transfer in a packed bed at very low channel to particle diameter ratio, *Chem. Eng. J.* 96 (1-3) (2003) 3–13, <https://doi.org/10.1016/j.ces.2003.08.026>.
- [9] M. Nijemeisland, A.G. Dixon, Comparison of CFD simulations to experiment for convective heat transfer in a gas-solid fixed bed, *Chem. Eng. J.* 82 (1-3) (2001) 231–246, [https://doi.org/10.1016/S1385-8947\(00\)00360-0](https://doi.org/10.1016/S1385-8947(00)00360-0).
- [10] A.G. Dixon, D.L. Cresswell, Theoretical prediction of effective heat transfer parameters in packed beds, *AIChE J.* 25 (4) (1979) 663–676, <https://doi.org/10.1002/aic.690250413>.
- [11] W.R. Paterson, J.J. Carberry, Fixed bed catalytic reactor modelling, *Chem. Eng. Sci.* 38 (1) (1983) 175–180, [https://doi.org/10.1016/0009-2509\(83\)80149-3](https://doi.org/10.1016/0009-2509(83)80149-3).
- [12] D. Vortmeyer, E. Haidegger, Discrimination of three approaches to evaluate heat fluxes for wall-cooled fixed bed chemical reactors, *Chem. Eng. Sci.* 46 (10) (1991) 2651–2660, [https://doi.org/10.1016/0009-2509\(91\)80058-7](https://doi.org/10.1016/0009-2509(91)80058-7).
- [13] E. Tsotsas, E.-U. Schlünder, Heat transfer in packed beds with fluid flow: remarks on the meaning and the calculation of a heat transfer coefficient at the wall, *Chem. Eng. Sci.* 45 (4) (1990) 819–837, [https://doi.org/10.1016/0009-2509\(90\)85005-X](https://doi.org/10.1016/0009-2509(90)85005-X).
- [14] M. Winterberg, E. Tsotsas, Modelling of heat transport in beds packed with spherical particles for various bed geometries and/or thermal boundary conditions, *Int. J. Therm. Sci.* 39 (5) (2000) 556–570, [https://doi.org/10.1016/S1290-0729\(00\)00251-9](https://doi.org/10.1016/S1290-0729(00)00251-9).
- [15] D. Wen, Y. Ding, Heat transfer of gas flow through a packed bed, *Chem. Eng. Sci.* 61 (11) (2006) 3532–3542, <https://doi.org/10.1016/j.ces.2005.12.027>.
- [16] A.G. Dixon, Fixed bed catalytic reactor modelling—the radial heat transfer problem, *Can. J. Chem. Eng.* 90 (3) (2012) 507–527, <https://doi.org/10.1002/cjce.21630>.

- [17] H. Freund, T. Zeiser, F. Huber, E. Klemm, G. Brenner, F. Durst, G. Emig, Numerical simulations of single phase reacting flows in randomly packed fixed-bed reactors and experimental validation, *Chem. Eng. Sci.* 58 (3-6) (2003) 903–910, [https://doi.org/10.1016/S0009-2509\(02\)00622-X](https://doi.org/10.1016/S0009-2509(02)00622-X).
- [18] M.E. Taskin, A.G. Dixon, M. Nijemeisland, E.H. Stitt, CFD Study of the Influence of Catalyst Particle Design on Steam Reforming Reaction Heat Effects in Narrow Packed Tubes, *Ind. Eng. Chem. Res.* 47 (16) (2008) 5966–5975, <https://doi.org/10.1021/ie800315d>.
- [19] Y. Dong, B. Sosna, O. Korup, F. Rosowski, R. Horn, B. Sosna, O. Korup, F. Rosowski, R. Horn, Investigation of radial heat transfer in a fixed-bed reactor : CFD simulations and profile measurements, *Chem. Eng. J.* 317 (2017) 204–214, <https://doi.org/10.1016/j.cej.2017.02.063>.
- [20] E.M. Moghaddam, E.A. Foumeny, A.I. Stankiewicz, J.T. Padding, Fixed bed reactors of non-spherical pellets : Importance of heterogeneities and inadequacy of azimuthal averaging, *Chem. Eng. Sci.* 1 (2019), 100006, <https://doi.org/10.1016/j.cesx.2019.100006>.
- [21] A.G. Dixon, G. Walls, H. Stanness, M. Nijemeisland, E.H. Stitt, Experimental validation of high Reynolds number CFD simulations of heat transfer in a pilot-scale fixed bed tube, *Chem. Eng. J.* 200-202 (2012) 344–356, <https://doi.org/10.1016/j.cej.2012.06.065>.
- [22] M. Behnam, A.G. Dixon, M. Nijemeisland, E.H. Stitt, A New Approach to Fixed Bed Radial Heat Transfer Modeling Using Velocity Fields from Computational Fluid Dynamics Simulations, *Ind. Eng. Chem. Res.* 52 (44) (2013) 15244–15261, <https://doi.org/10.1021/ie4000568>.
- [23] E.M. Moghaddam, E.A. Foumeny, A.I. Stankiewicz, J.T. Padding, Rigid Body Dynamics Algorithm for Modeling Random Packing Structures of Nonspherical and Nonconvex Pellets, *Ind. Eng. Chem. Res.* 57 (44) (2018) 14988–15007, <https://doi.org/10.1021/acs.iecr.8b03915.s002>.
- [24] A.G. Dixon, The length effect on packed bed effective heat transfer parameters, *Chem. Eng. J.* 31 (3) (1985) 163–173, [https://doi.org/10.1016/0300-9467\(85\)80057-5](https://doi.org/10.1016/0300-9467(85)80057-5).
- [25] M.G. Freiwald, W.R. Paterson, Accuracy of model predictions and reliability of experimental data for heat transfer in packed beds, *Chem. Eng. Sci.* 47 (7) (1992) 1545–1560, [https://doi.org/10.1016/0009-2509\(92\)85003-T](https://doi.org/10.1016/0009-2509(92)85003-T).
- [26] Y. Ding, Z. Wang, D. Wen, M. Ghadiri, X. Fan, D. Parker, Solids behaviour in a gas–solid two-phase mixture flowing through a packed particle bed, *Chem. Eng. Sci.* 60 (19) (2005) 5231–5239, <https://doi.org/10.1016/j.ces.2005.04.052>.
- [27] T. Eppinger, K. Seidler, M. Kraume, DEM-CFD simulations of fixed bed reactors with small tube to particle diameter ratios, *Chem. Eng. J.* 166 (1) (2011) 324–331, <https://doi.org/10.1016/j.cej.2010.10.053>.
- [28] A. Singhal, S. Cloete, S. Radl, R. Quinta-Ferreira, S. Amini, Heat transfer to a gas from densely packed beds of monodisperse spherical particles, *Chem. Eng. J.* 314 (2017) 27–37, <https://doi.org/10.1016/j.cej.2016.12.124>.
- [29] Z. Guo, Z. Sun, N. Zhang, M. Ding, Y. Zhou, Influence of flow guiding conduit on pressure drop and convective heat transfer in packed beds, *Int. J. Heat Mass Transf.* 134 (2019) 489–502, <https://doi.org/10.1016/j.jheatmasstransfer.2019.01.066>.
- [30] S. Bale, M. Sathe, O. Ayeni, A.S. Berrouk, J. Joshi, K. Nandakumar, Spatially resolved mass transfer coefficient for moderate Reynolds number flows in packed beds: Wall effects, *Int. J. Heat Mass Transf.* 110 (2017) 406–415, <https://doi.org/10.1016/j.jheatmasstransfer.2017.03.052>.
- [31] S. Bale, S. Tiwari, M. Sathe, A.S. Berrouk, K. Nandakumar, J. Joshi, Direct numerical simulation study of end effects and D/d ratio on mass transfer in packed beds, *Int. J. Heat Mass Transf.* 127 (2018) 234–244, <https://doi.org/10.1016/j.jheatmasstransfer.2018.07.100>.
- [32] A.G. Dixon, M. Nijemeisland, CFD as a Design Tool for Fixed-Bed Reactors, *Ind. Eng. Chem. Res.* 40 (23) (2001) 5246–5254, <https://doi.org/10.1021/ie001035a>.
- [33] G.D. Wehinger, M. Kraume, V. Berg, O. Korup, K. Mette, R. Schögl, M. Behrens, R. Horn, Investigating dry reforming of methane with spatial reactor profiles and particle-resolved CFD simulations, *AIChE J.* 62 (12) (2016) 4436–4452, <https://doi.org/10.1002/aic.15520>.
- [34] H. Bai, Jörg Theuerkauf, P.A. Gillis, P.M. Witt, A Coupled DEM and CFD Simulation of Flow Field and Pressure Drop in Fixed Bed Reactor with Randomly Packed Catalyst Particles, *Ind. Eng. Chem. Res.* 48 (8) (2009) 4060–4074, <https://doi.org/10.1021/ie801548h>.
- [35] A. Singhal, S. Cloete, S. Radl, R. Quinta-Ferreira, S. Amini, Heat transfer to a gas from densely packed beds of cylindrical particles, *Chem. Eng. Sci.* 172 (2017) 1–12, <https://doi.org/10.1016/j.ces.2017.06.003>.
- [36] G.D. Wehinger, C. Fütterer, M. Kraume, Contact Modifications for CFD Simulations of Fixed-Bed Reactors: Cylindrical Particles, *Ind. Eng. Chem. Res.* 56 (1) (2017) 87–99, <https://doi.org/10.1021/acs.iecr.6b03596>.
- [37] G. Ruiz, N. Ripoll, N. Fedorova, A. Zbogar-Rasic, V. Jovicic, A. Delgado, M. Toledo, Experimental and numerical analysis of the heat transfer in a packed bed exposed to the high thermal radiation flux, *Int. J. Heat Mass Transf.* 136 (2019) 383–392, <https://doi.org/10.1016/j.jheatmasstransfer.2019.03.009>.
- [38] H. Freund, J. Bauer, T. Zeiser, G. Emig, Detailed Simulation of Transport Processes in Fixed-Beds, *Ind. Eng. Chem. Res.* 44 (16) (2005) 6423–6434, <https://doi.org/10.1021/ie0489453>.
- [39] M.J. Baker, P.G. Young, G.R. Tabor, Image based meshing of packed beds of cylinders at low aspect ratios using 3d MRI coupled with computational fluid dynamics, *Comput. Chem. Eng.* 35 (10) (2011) 1969–1977, <https://doi.org/10.1016/j.compchemeng.2011.03.017>.
- [40] G. Boccardo, F. Augier, Y. Haroun, D. Ferré, D.L. Marchisio, Validation of a novel open-source work-flow for the simulation of packed-bed reactors, *Chem. Eng. J.* 279 (2015) 809–820, <https://doi.org/10.1016/j.cej.2015.05.032>.
- [41] B. Partopour, A.G. Dixon, Resolved-particle fixed bed CFD with microkinetics for ethylene oxidation, *AIChE J.* 63 (1) (2017) 87–94, <https://doi.org/10.1002/aic.15422>.
- [42] S. Rebughini, A. Cuoci, M. Maestri, Handling contact points in reactive CFD simulations of heterogeneous catalytic fixed bed reactors, *Chem. Eng. Sci.* 141 (2016) 240–249, <https://doi.org/10.1016/j.ces.2015.11.013>.
- [43] G.D. Wehinger, T. Eppinger, M. Kraume, Detailed numerical simulations of catalytic fixed-bed reactors: Heterogeneous dry reforming of methane, *Chem. Eng. Sci.* 122 (2015) 197–209, <https://doi.org/10.1016/j.ces.2014.09.007>.
- [44] A.G. Dixon, CFD study of effect of inclination angle on transport and reaction in hollow cylinder catalysts, *Chem. Eng. Res. Des.* 92 (7) (2014) 1279–1295, <https://doi.org/10.1016/j.cherd.2013.11.018>.
- [45] F. Augier, F. Idoux, J.Y. Delenne, Numerical simulations of transfer and transport properties inside packed beds of spherical particles, *Chem. Eng. Sci.* 65 (3) (2010) 1055–1064, <https://doi.org/10.1016/j.ces.2009.09.059>.
- [46] S.G. Kim, Y. Addad, M. Liu, J.I. Lee, Y. Lee, Computational investigation into heat transfer coefficients of randomly packed pebbles in flowing FLiBe, *Int. J. Heat Mass Transf.* 145 (2019) 118769, <https://doi.org/10.1016/j.jheatmasstransfer.2019.118769>.
- [47] G.D. Wehinger, T. Eppinger, M. Kraume, Evaluating catalytic fixed-bed reactors for dry reforming of methane with detailed CFD, *Chem.-Ing.-Tech.* 87 (2015), <https://doi.org/10.1002/cite.201400153>.
- [48] B. Partopour, A.G. Dixon, An integrated workflow for resolved-particle packed bed models with complex particle shapes, *Powder Technol.* 322 (2017) 258–272, <https://doi.org/10.1016/j.powtec.2017.09.009>.
- [49] W. Zhong, A. Yu, X. Liu, Z. Tong, H. Zhang, DEM/CFD-DEM Modelling of Non-spherical Particulate Systems: Theoretical Developments and Applications, *Powder Technol.* 302 (2016) 108–152, <https://doi.org/10.1016/j.powtec.2016.07.010>.
- [50] L.J.H. Seelen, J.T. Padding, J.A.M. Kuipers, A granular Discrete Element Method for arbitrary convex particle shapes: Method and packing generation, *Chem. Eng. Sci.* 189 (2018) 84–101, <https://doi.org/10.1016/j.ces.2018.05.034>.
- [51] S. Flaischlen, G.D. Wehinger, Synthetic Packed-Bed Generation for CFD Simulations: Blender vs. STAR-CCM+, *ChemEngineering*. 3 (2019) 52, <https://doi.org/10.3390/chemengineering3020052>.
- [52] E.M. Moghaddam, A. Farbod, A Novel Approach in Modelling Narrow-Tube Fixed Bed Reactors: The Role of Tortuous Structure on Transport Properties, *Eur. Symp. Chem. React. Eng.* 2015. (2015) Munich, Germany.
- [53] C. Loop, Smooth subdivision surfaces based on triangles, *The University of Utah*, 1987.
- [54] A.G. Dixon, M. Nijemeisland, E.H. Stitt, Systematic mesh development for 3D CFD simulation of fixed beds: Contact points study, *Comput. Chem. Eng.* 48 (2013) 135–153, <https://doi.org/10.1016/j.compchemeng.2012.08.011>.
- [55] H.P.A. Calis, J. Nijenhuis, B.C. Paikert, F.M. Dautzenberg, C.M. Van Den Bleek, CFD modeling and experimental validation of pressure drop and flow profile in a novel structured catalytic reactor packing, *Chem. Eng. Sci.* 56 (2001) 1713–1720, [https://doi.org/10.1016/S0009-2509\(00\)00400-0](https://doi.org/10.1016/S0009-2509(00)00400-0).
- [56] A. Guardo, M. Coussirat, F. Recasens, M.A. Larrayoz, X. Escaler, CFD study on particle-to-fluid heat transfer in fixed bed reactors: Convective heat transfer at low and high pressure, *Chem. Eng. Sci.* 61 (13) (2006) 4341–4353, <https://doi.org/10.1016/j.ces.2006.02.011>.
- [57] A.G. Dixon, Correlations for wall and particle shape effects on fixed bed bulk voidage, *Can. J. Chem. Eng.* 66 (5) (1988) 705–708, <https://doi.org/10.1002/cjce:5450660501>.
- [58] G.E. Mueller, Angular void fraction distributions in randomly packed fixed beds of uniformly sized spheres in cylindrical containers, *Powder Technol.* 77 (3) (1993) 313–319, [https://doi.org/10.1016/0032-5910\(93\)85023-3](https://doi.org/10.1016/0032-5910(93)85023-3).
- [59] P.J. Roache, Verification of Codes and Calculations, *AIAA J.* 36 (5) (1998) 696–702, <https://doi.org/10.2514/2.457>.
- [60] D. Mehta, M.C. Hawley, Wall Effect in Packed Columns, *Ind. Eng. Chem. Proc. Des. Dev.* 8 (2) (1969) 280–282, <https://doi.org/10.1021/i260030a021>.
- [61] W. Reichelt, Zur Berechnung des Druckverlustes einphasig durchströmter Kugel- und Zylinderschüttungen, *Chemie Ing. Techn.* 44 (18) (1972) 1068–1071, <https://doi.org/10.1002/cite.330441806>.
- [62] E.A. Foumeny, F. Benyahia, J.A.A. Castro, H.A. Moallemi, S. Roshani, Correlations of pressure drop in packed beds taking into account the effect of confining wall, *Int. J. Heat Mass Transf.* 36 (2) (1993) 536–540, [https://doi.org/10.1016/0017-9310\(93\)80028-S](https://doi.org/10.1016/0017-9310(93)80028-S).
- [63] B. Eisefeld, K. Schnitzlein, The influence of confining walls on the pressure drop in packed beds, *Chem. Eng. Sci.* 56 (14) (2001) 4321–4329, [https://doi.org/10.1016/S0009-2509\(00\)00533-9](https://doi.org/10.1016/S0009-2509(00)00533-9).
- [64] A. Montillet, E. Akkari, J. Comiti, About a correlating equation for predicting pressure drops through packed beds of spheres in a large range of Reynolds numbers, *Chem. Eng. Process. Process Intensif.* 46 (4) (2007) 329–333, <https://doi.org/10.1016/j.cep.2006.07.002>.
- [65] D. Nemeč, J. Levec, Flow through packed bed reactors: 1. Single-phase flow, *Chem. Eng. Sci.* 60 (24) (2005) 6947–6957, <https://doi.org/10.1016/j.ces.2005.05.068>.
- [66] N.-S. Cheng, Wall effect on pressure drop in packed beds, *Powder Technol.* 210 (3) (2011) 261–266, <https://doi.org/10.1016/j.powtec.2011.03.026>.
- [67] G. Sonntag, Einfluß des Lückenvolumens auf den Druckverlust in gasdurchströmten Füllkörpersäulen: Einfluß des Lückenvolumens auf den Druckverlust in gasdurchströmten Füllkörpersäulen, *Chem. Ing. Techn.* 32 (5) (1960) 317–329, <https://doi.org/10.1002/cite.330320502>.
- [68] S.N. Gunn, Fluid flow through packed columns, *Chem. Eng. Prog.* 48 (1952) 89–94.
- [69] S.E. Gupta, R.B. Chaube, S.N. Upadhyay, Fluid-particle and heat transfer beds, *Chem. Eng.* 29 (1974) 839–843.

- [70] D.J. Gunn, Transfer of heat or mass to particles in fixed and fluidised beds, *Int. J. Heat Mass Transf.* 21 (4) (1978) 467–476, [https://doi.org/10.1016/0017-9310\(78\)90080-7](https://doi.org/10.1016/0017-9310(78)90080-7).
- [71] N. Wakao, S. Kagueli, T. Funazkri, Effect of fluid dispersion coefficients on particle-to-fluid heat transfer coefficients in packed beds, *Chem. Eng. Sci.* 34 (3) (1979) 325–336, [https://doi.org/10.1016/0009-2509\(79\)85064-2](https://doi.org/10.1016/0009-2509(79)85064-2).
- [72] B. Sun, S. Tenneti, S. Subramaniam, Modeling average gas–solid heat transfer using particle-resolved direct numerical simulation, *Int. J. Heat Mass Transf.* 86 (2015) 898–913, <https://doi.org/10.1016/j.ijheatmasstransfer.2015.03.046>.
- [73] B. Stuke, Wärmeaustausches in Regeneratoren mit zylindrischem, *Angew. Chemie.* 10 (1948) 262–268.
- [74] E.M. Moghaddam, E.A. Foumeny, A.I. Stankiewicz, J.T. Padding, Hydrodynamics of narrow-tube fixed bed reactors filled with Raschig rings, *Chem. Eng. Sci.*: X 5 (2020) 100057, <https://doi.org/10.1016/j.cesx.2020.100057>.
- [75] Y. Dong, M. Geske, O. Korup, N. Ellenfeld, F. Rosowski, C. Dobner, R. Horn, What happens in a catalytic fixed-bed reactor for n-butane oxidation to maleic anhydride? Insights from spatial profile measurements and particle resolved CFD simulations, *Chem. Eng. J.* 350 (2018) 799–811, <https://doi.org/10.1016/j.cej.2018.05.192>.
- [76] J.J. Lerou, G.F. Froment, Estimation of heat transfer parameters in packed beds from radial temperature profiles, *Chem. Eng. J.* 15 (3) (1978) 233–237, [https://doi.org/10.1016/0300-9467\(78\)80008-2](https://doi.org/10.1016/0300-9467(78)80008-2).
- [77] A.P. de Wasch, G.F. Froment, Heat transfer in packed beds, *Chem. Eng. Sci.* 27 (3) (1972) 567–576, [https://doi.org/10.1016/0009-2509\(72\)87012-X](https://doi.org/10.1016/0009-2509(72)87012-X).
- [78] J.J. Lerou, G.F. Froment, Velocity, temperature and conversion profiles in fixed bed catalytic reactors, *Chem. Eng. Sci.* 32 (8) (1977) 853–861, [https://doi.org/10.1016/0009-2509\(77\)80071-7](https://doi.org/10.1016/0009-2509(77)80071-7).
- [79] M. Flávio Pinto Moreira, M. do Carmo Ferreira, J.T. Freire, Evaluation of pseudohomogeneous models for heat transfer in packed beds with gas flow and gas–liquid cocurrent downflow and upflow, *Chem. Eng. Sci.* 61 (6) (2006) 2056–2068, <https://doi.org/10.1016/j.ces.2005.11.003>.
- [80] R. Henda, A. Machac, B. Nilsson, Heat and mass transport in a nonlinear fixed-bed catalytic reactor: Hot spots and thermal runaway, *Chem. Eng. J.* 143 (1-3) (2008) 195–200, <https://doi.org/10.1016/j.cej.2008.04.015>.
- [81] F. Manenti, S. Cieri, M. Restelli, G. Bozzano, Dynamic modeling of the methanol synthesis fixed-bed reactor, *Comput. Chem. Eng.* 48 (2013) 325–334, <https://doi.org/10.1016/j.compchemeng.2012.09.013>.
- [82] M. Winterberg, E. Tsotsas, Correlations for effective heat transport coefficients in beds packed with cylindrical particles, *Chem. Eng. Sci.* 55 (23) (2000) 5937–5943, [https://doi.org/10.1016/S0009-2509\(00\)00198-6](https://doi.org/10.1016/S0009-2509(00)00198-6).
- [83] P. Zehner, E.U. Schlünder, Wärmeleitfähigkeit von Schüttungen bei mäßigen Temperaturen: Wärmeleitfähigkeit von Schüttungen bei mäßigen Temperaturen, *Chem. Ing. Tech.* 42 (14) (1970) 933–941, <https://doi.org/10.1002/cite.330421408>.